Global characterization of oscillating grid turbulence in homogeneous and two-layer fluids, and its implication for mixing at high Peclet number

Marie Poulain-Zarcos, Matthieu Mercier, Alexandra ter Halle

Global characterization of oscillating grid turbulence in homogeneous and two-layer fluids, and its implication for mixing at high Peclet number

Marie Poulain-Zarcos*
Institut de Mécanique des Fluides de Toulouse, (IMFT), Université de Toulouse, CNRS, Allée du Professeur Camille Soula, 31400 Toulouse, France and Laboratoire des IMRCP, Université de Toulouse, CNRS UMR 5623, Université Paul Sabatier, 118 route de Narbonne 31062 Toulouse Cedex 9, France

Matthieu J. Mercier†
Institut de Mécanique des Fluides de Toulouse, (IMFT), Université Toulouse, CNRS, Allée du Professeur Camille Soula, 31400 Toulouse, France

Alexandra ter Halle
Laboratoire des IMRCP, Université de Toulouse, CNRS UMR 5623, Université Paul Sabatier, 118 route de Narbonne 31062 Toulouse Cedex 9, France
(Dated: March 27, 2022)

Oscillating grid turbulence (OGT) is a specific situation allowing to investigate the equilibrium between the turbulent kinetic energy, k, and the dissipation rate, ϵ, without any mean flow. One of its main features is that, in homogeneous fluids, the turbulence intensity decreases with the distance to the vibrating grid used to generate the forcing. OGT is thus usually described in terms of depth profiles of turbulent quantities. In this paper, we discuss experiments realized in two different setups and compare our results for all turbulent quantities with past studies. The results on the turbulent kinetic energy and the integral length scale lead us to propose a parametric model for the eddy viscosity, ν_t, taking into account the spatial decay of the turbulence being slightly different than previous descriptions. Indeed, we find that ν_t is best described as a constant value over a certain depth, H_s, before decreasing quickly as a power law in $z^{-3/2}$. The specific depth H_s is defined at the depth where a discontinuity of the integral length scale is observed. Physically, it corresponds to the depth at which the presence of the grid no longer influences the flow. We also describe OGT in the case of a two-layer fluid. The description of the turbulence at depths z far from the position of the interface h ($0 < z/h < 0.6$) is very similar to the case of an homogeneous fluid, whereas the region near the interface ($0.6 < z/h < 1$) is strongly altered by the presence of the fluid boundary. Surprisingly, ν_t (at the difference of the others turbulent quantities) no longer depends on z in such configuration. Finally, we investigate mixing processes at the interface in this context. Thanks to large field measurement (about the width of the tank), we were able to identify large scale coherent structures as well as the turbulent flow. We discuss the entrainment law of the interface, and its relationship with the Richardson number based on different definitions used in previous studies, as well as by using our observations of the turbulent flow properties at the interface. Our observations suggest that mixing at the interface in OGT is controlled by the turbulent flow properties at the interface but could also be influenced by weak mean flow features, this could explain the difficulty to discriminate a simple dependency of the entrainment rate with the Richardson number.

Keywords: grid turbulence, decaying turbulence, stratified turbulence, mixing.

I. INTRODUCTION

Oscillating grid turbulence (OGT) is a well-characterized type of turbulent flow, both for homogeneous and stratified fluids. For example, oscillating grid systems are used to simulate the turbulence induced by waves and wind which are the main source of mixing in the upper layer of the ocean [1, 2]. It is also used to study sediment or pollutant transport in homogeneous fluid based on the equilibrium between advection and diffusion processes [3–6].

The main results first shown by Thompson and Turner [7] and Hopfinger and Toly [8] is that the Root Mean Square (RMS) velocities in the x (horizontal) and z (vertical) directions, respectively U_{rms} and W_{rms}, decrease with the power law z^n in a homogeneous fluid [7, 8]. For grid with square bars, Thompson and Turner [7] found an exponent $n = -1.5$ starting from the mean position of the grid, while Hopfinger and Toly [8] found an exponent $n = -1$ starting

* marie.poulain.1@univ-amu.fr; currently at Aix-Marseille Univ., France
† matthieu.mercier@imft.fr

from a virtual origin, z_v, defined as the position at which the integral length-scale, L_{int}, becomes zero. This virtual origin is generally below the mean position of the grid at $S/2 + 1 \pm 0.5$ cm, where S is the stroke [8]. de Silva and Fernando [9] mentioned that the exponent n is very sensitive to the origin of z taken and they advised to use the virtual origin. However, several studies considered the mean position of the grid as the origin of z [4, 10, 11]. In the following, we will express all depth profiles from the distance of z_v. In our case, we note z the distance from z_v and z' the distance from the top position of the grid. In such convention, the RMS velocities depth profiles can be parametrized by

$$< U_{rms} >_x = C_1 M^{1/2} S^{3/2} f_g z^{-1} \quad \text{and} \quad < W_{rms} >_x = C_2 M^{1/2} S^{3/2} f_g z^{-1}\,, \tag{1}$$

where M is the grid mesh and C_1 and C_2 are constants varying between 0.20 and 0.25 and 0.19 and 0.27 respectively [8, 9, 12]. These constants might depend on S and f_g, the grid frequency, however, no clear relation is established for now and most of authors assume C_1 and C_2 as constant [8, 13]. Based on eq. (1) and assuming a local isotropy in the horizontal plane, the turbulent kinetic energy (TKE), $k = \overline{u'^2} + 0.5\overline{w'^2}$, can be parametrized by [14] :

$$k = 0.5(2C_1 + C_2)^2 M S^3 f_g^2 z^{-2}\,. \tag{2}$$

Another modeling approach proposed by Matsunaga *et al.* [10] is based on analytical developments using a $k - \epsilon$ model for turbulence. Notably, the authors obtained a parametric law for k, which he considered to better describe the TKE over the entire water column,

$$k = k_0 \left[\frac{\epsilon_0}{1.82 k_0^{1.5}} z + 1 \right]^{-5}\,, \tag{3}$$

with k_0 and ϵ_0 the turbulent kinetic energy and the dissipation rate injected in the system by the grid respectively. Depending on the value of the grid Reynolds number $Re_g = f_g S^2/\nu_f$, where ν_f is the kinematic viscosity of the fluid, one can write

$$k_0 = 0.0081 M^{-1/4} S^{9/4} f_g^2 Re_g^{1/2} \quad \text{and} \quad \epsilon_0 = 0.082 M^{-1} S^3 f_g^3 Re_g \quad \text{for} \quad Re_g < 5500\,, \tag{4}$$

$$k_0 = 0.6 M^{-1/4} S^{9/4} f_g^2 \quad \text{and} \quad \epsilon_0 = 0.45 M^{-1} S^3 f_g^3 \quad \text{for} \quad Re_g > 5500\,. \tag{5}$$

In the following, we define $L_{\epsilon-k} = 1.82 k_0^{1.5}/\epsilon_0$, a characteristic length-scale convenient to compare with observations. Recently, Rastello *et al.* [11] revised the model of Matsunaga *et al.* [10]. They supply a slightly different definition for k_0 and ϵ_0 at low Reynolds number (< 1000). These modeling approaches allow to predict the vertical dependencies of other characteristic quantities such as the TKE flux, the dissipation rate ϵ, or the turbulent eddy viscosity ν_t.

Concerning the integral length scale, both the analytical predictions and direct observations suggest that

$$L_{int} = \beta z' + z_v \tag{6}$$

with β an experimental constant being approximately 0.1 [7–9, 15, 16]. Although it was shown that β might depends on S and might be higher near the grid, β is generally considered constant [13, 17].

OGT was also used to understand processes in stratified fluids, with the first study of Rouse and Dodu [18]. Especially some authors studied the evolution of the entrainment velocity, U_e, in two-layer fluids configurations [7, 8, 16, 19–21]. Indeed, even if the deep ocean is linearly stratified, the presence a sharp density can exist near the surface due to thermal effects essentially, impacting the vertical mixing of the upper ocean [22]. Typically, the interface can be seen as a wall for the vertical transport of turbulence. Consequently, there is a transfer from vertical to horizontal scales with a flattening of turbulent eddies near the interface; the flow is not isotropic any more and the transversal component, U_{rms}, is amplified [23]. Nevertheless, some mixing occurs with the position of the interface evolving slowly (compared to the grid frequency) with time. The entrainment rate, E, is defined as the ratio of the entrainment velocity, $U_e = \mathrm{d}h/\mathrm{d}t$, and a characteristic velocity of the turbulent flow at the interface, U_{rms}. Turner [24] was one of the first to propose an evolution of the entrainment rate as a function of the properties of the turbulent stratified flow prescribed by S, f_g, L_{int}, the density difference between the two fluid layers, $\Delta\rho = \rho_2 - \rho_1$, the position of the interface (or mixing layer), h, and the diffusivity of the stratifying agent κ. This dependence was largely investigated since this work [3, 8, 15, 16, 21, 24–26], suggesting that the E should be a function of the overall Richardson number Ri defined as $\Delta\rho g L_{int}/\rho_1 U_{rms}^2$, and of the Peclet number $Pe = (\nu_f/\kappa)Re$, if the value for the latter is smaller than $\sim 10^3$ [19, 24, 27]. In the specific case of a salinity density gradient studied in our work, the dependency with the Pe number can be neglected and the following relationship is proposed

$$E \propto Ri^{\gamma}\,. \tag{7}$$

As a remark, a value of $-3/2$ for γ is found considering an appropriate Richardson number for each study [1], that-is-to-say by choosing the adequate turbulent quantities in the definition of Ri. Nevertheless, it must be noted that these turbulent quantities are always estimated (or measured) in homogeneous fluid conditions. Thus the exponent of this power law is still an open question, especially for small Ri. Indeed, if $Ri < 5$ a smaller value of -1.2 can be found for γ [15]. The entrainment law is based upon the theoretical assumption that mixing occurs by local interfacial instabilities and intermittent mixing processes induced by interfacial waves breaking initiated by turbulent eddies or instabilities, as described in Fernando and Hunt [28] for instance, when the Richardson is sufficiently large. The limit of E for very large values for Ri is also not adequately modeled by eq.(7), which should be independent of Ri [24, 26].

In this paper, we use Particle Image Velocimetry measurements (PIV) to propose a revised parametric description of relevant turbulent quantities for OGT in a homogeneous and a two-layer stratified fluid, with the ultimate goal to parameterize the eddy viscosity which has not been considered in previous work. We also investigate the mixing of the two-layer stratified case using experimental observations (PIV and density measurements). In Section II, we present the experimental setup and methods used in this study. Then, in a Section III we discuss past models used to describe OGT in homogeneous fluid and we proposed a simplified eddy viscosity model. In Section IV, we discuss in what extent OGT is modified in a two-layer fluid. Finally, we discuss in Section V the mixing induced at the interface, before concluding.

II. EXPERIMENTAL SETUP AND METHODOLOGY

A. Experimental setup

The study has been performed in two experimental setups. The biggest one, with a glass tank of $1\times1\times1$ m^3, is shown in Fig. 1. The smallest one has a tank with a height of 1.2 m and a cross section of 0.4×0.4 m^2. In the following, setup 1 will refer to the biggest tank and setup 2 to the smallest one.

In both cases, the glass tank is filled with salt water (NaCl) and the turbulence is generated by an oscillating grid. The highest position of the grid is kept 1.7 cm below the water surface. The water depth is 0.95 m in setup 1 and 1.00 m in setup 2. The grid is made of square bars of width $M/5$ with M the grid mesh ($M = 10$ cm in setup 1 and $M = 5$ cm in setup 2). The solidity of the grid is 34 % (respectively 36 %) in setup 1 (respectively 2). These values, below 40 %, ensure the ability to minimize secondary flows [8, 9, 29]. As mentioned before, the grid oscillates vertically at the frequency f_g with a stroke S. Based on these two parameters, a Reynolds number is defined to characterize the stirring, $Re_g = f_g S^2/\nu_f$, with ν_f the kinematic viscosity of the fluid. Experimental parameters are reported in Table I.

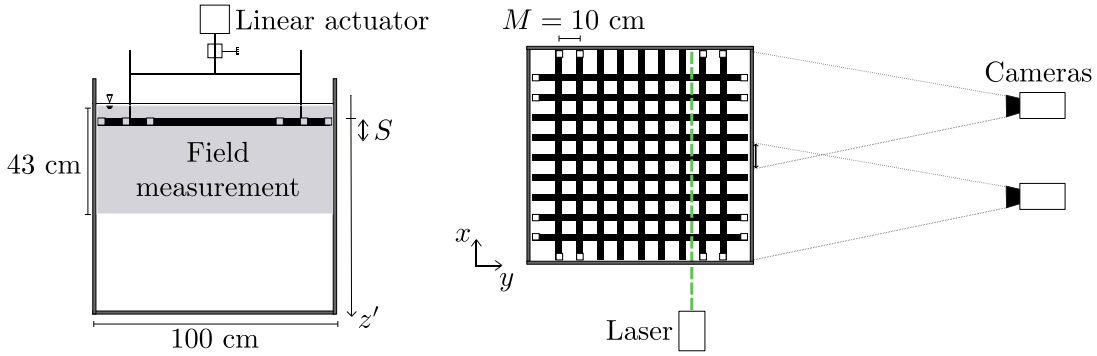

FIG. 1. Sketch of experimental setup 1.

In homogeneous fluid, the water density is $\rho_f = 1042.0$ kg/m^3. In two-layer fluids, the upper layer is saline water with a density ρ_1 and the bottom one with a density ρ_2 with $\rho_2 > \rho_1$. Before initiating the stirring, the interface is at $h = 20$ cm below the water surface and the density difference between the two fluid layers is $\Delta\rho_{0i} = \rho_2(t = 0) - \rho_1(t = 0)$ kg/m^3, with $i = \{1, 2\}$ indicating different initial conditions as reported in Table I. In order to avoid distortion of the laser sheet and scatter of the light, an index matching technique is carried out in the two-layer fluid configuration. It consists in adding ethanol in the proper proportions in the lightest fluid to have the desired density ρ_1 with the same refractive index as the bottom layer. Here, since we have small density differences (but strong gradients), we add between 2 and 3 % in mass ethanol to reach a refractive index of 1.3434 ± 0.0003.

♯	S (cm)	f_g (Hz)	Re_g	Set up	Fluid	$\Delta\rho_{01}$ (kg/m^3)	$\Delta\rho_{02}$ (kg/m^3)	Number of runs with $k/K > 10$ (Total number of runs)
H1	8	2	12 550	2	Homogeneous	0	0	0 (4)
H2	6	2	7 190	2	Homogeneous	0	0	0 (4)
H3	4	5	7 980	2	Homogeneous	0	0	5 (6)
H4		3	4 790	2	Homogeneous	0	0	5 (6)
H5		2	3 190	2	Homogeneous	0	0	1 (6)
H6		1.5	2 400	1	Homogeneous	0	0	1 (1)
H7		0.75	1 200	2	Homogeneous	0	0	4 (4)
H8	3.4	1.5	1 730	1	Homogeneous	0	0	1 (1)
H9	2	7	2 790	2	Homogeneous	0	0	2 (4)
H10		5	1 200	2	Homogeneous	0	0	1 (6)
H11		2	800	2	Homogeneous	0	0	1 (6)
H12		2	800	1	Homogeneous	0	0	1 (1)
H13	1.4	3	590	1	Homogeneous	0	0	0 (1)
S1	4	1.5	2 400	1	Two-layer	2.8	–	2 (2)
S2	3.4	1.5	1 730	1	Two-layer	2.2	1.1	2 (2)
S3	2	2	800	1	Two-layer	3.2	1.8	2 (2)
S4	1.4	3	590	1	Two-layer	3	1.2	2 (2)

TABLE I. Experimental parameters (S is the stroke, f_g is the oscillating frequency, Re_g is the Reynolds number based on the stirring and $\Delta\rho_{0i}$ is the initial density difference).

B. Conductivity measurements

In the two-layer fluid, due to the turbulent forcing of the interface, mixing occurs in the upper layer with an increase of ρ_1 with time and a modification of the position and shape of the interface. To measure it, density profiles are recorded using a conductivity and temperature probe (MSCTI probe from PME©) in addition to PIV measurements described in §II C. The conductivity probe is mounted on a motor-controlled translating shaft, hence moves vertically from the water surface to 55 cm below it with a fixed speed of 5 mm/s to avoid disturbing the flow. The probe records samples at 500 Hz which leads to a spatial resolution of 10 μm ; however smoothing of the data in time (over 50 samples) is still made to reduce the level of noise, leading to an apparent resolution of 0.5 mm. The calibration in density is made before each experimental run, using 6 water samples with different densities encompassing the water density in the tank, while the calibration in temperature is valid for several days. For each experiment, 7 density profiles are recorded : 3 in a 'short' interval of time (t_1 before the beginning of the stirring, $t_2 = 17$ min, $t_3 = 30$ min after initiation of the stirring) and 4 after a larger period of time ($t_4 = 1$ h, $t_5 = 2$ h, $t_6 = 3$ h and $t_7 = 4$ h). An example of a density profile obtained is shown in Fig. 2.(a). The position of the interface, h, as a function of time can be obtained from different definitions. One can use the position of the maximum value of the Brunt-Väisälä frequency, $N^2 = -g\partial\rho/\partial z/ < \rho >_z$, with g the gravitational acceleration and $< \rho >_z$ the vertical average of the water density. Alternatively, the definitions can be based on the depth of the mean density $(\rho_1 + \rho_2)/2$ or on the mean depth of the density jump $(z_1 + z_2)/2$, with z_1 such as $\rho(z_1) = 1.15\rho_1$ and z_2 such as $\rho(z_2) = 0.85\rho_2$. These values can differ since the density profile is not symmetrical, the largest differences in h between all these definitions is about 5% at the initial time step and decreases after 15 min of stirring until less than 2 % (not shown here). In the following, we define h as the altitude where the Brunt-Väisälä frequency is maximum.

C. PIV measurements

The PIV field of view (almost 45 cm in height, over the full width of the tank in both setup), shown in Fig. 1 by the shaded area, is illuminated by a laser sheet (CFR 200 laser source, wavelength of 532 nm, 200mJ max.). In setup 1, it is fixed and located at $x/L = 1/4$ from the border of the tank. In setup 2, the laser sheet is translated by a translating stage to allow measurements at $x/L = 1/4$ and $x/L = 1/2$. In both setup, the laser sheet thickness is approximately 1 mm.

To visualize the whole tank width with the same spatial resolution for the two setups, images are recorded using two sCMOS cameras mounted side-by-side, with a resolution of 2160×2560 pixels, in setup 1, and by only one camera

in setup 2. They are located at 6.5 m (resp. 3.5 m) from the front face of the tank in setup 1 (resp. 2), leading to a field of view for each camera of 43×52 cm^2 (resp. 45×40 cm^2) with an overlap of one mesh size (Fig. 1) between the two cameras. In setup 1, the spatial resolution for each camera being 210 μm/pixel, spherical particles of polystyrene ($\rho_p \sim 1060$ kg/m^3) with a diameter of 228 μm are used to characterize the flow. We verified that the particles are between 1.5 and 4 times smaller than the Kolmogorov scale. In setup 2, the spatial resolution is 179 μm, we use spherical particles encapsulated by rhodamine with a diameter of 50 μm as tracers (their diameter being between 7 and 30 times smaller than the Kolmogorov scale). Thus they are tracers of the flow even if they are much larger than classical PIV particles [13, 30, 31]. To reduce their settling velocity, salt water is used even in homogeneous fluid.

In order to resolve the oscillatory grid dynamics, especially just under the grid, the acquisition is done in sequential mode ($Re_g < 3000$) or in double burst mode ($Re_g > 3000$) depending on the stirring. Far away from the grid, the time step is increased artificially during the post-processing in order to decrease the relative error on the displacement calculation, and thus on the velocity field. Typical values for the time step are chosen to achieve a mean displacement of 8 pixels at 30 cm below the water surface. The velocity fields are calculated using Lavision software from Davis©. The final step of computations corresponds to interrogation windows of 16 × 16 pixels with an overlap of 50 %. The spatial resolution obtained is 0.17×0.17 cm^2 in setup 1 and 0.14×0.14 cm^2 in setup 2. The reconstruction of a snapshot of the horizontal velocity field, u is shown Fig. 2(b), where the velocity fields from the two cameras in setup 1 are merged by averaging the velocity in the overlapping area of one mesh size as mentioned before. It corresponds to grid parameters with $Re_g = 800$, in the two-layer fluid configuration, 30 min after the beginning of the experiment (case S3). The interface is located at 26 cm from the water surface as shown in Fig. 2(a).

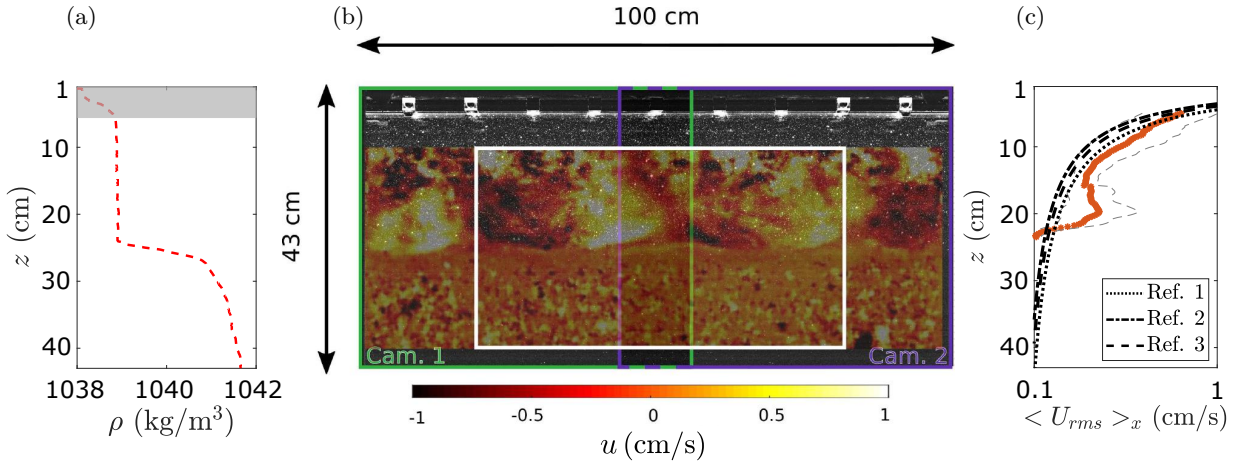

FIG. 2. (a) Density vertical profile from conductivity measurements. (b) Snapshot of the horizontal velocity field reconstructed after calculation. The green/violet rectangles are the views from cameras 1/2. The white rectangle indicates the area used to average turbulent quantities in the x direction. (c) Vertical profile of the horizontal RMS velocity in the upper layer. Symbols are experimental data and dark lines are classical laws used in homogeneous flow. Ref 1 to 3 correspond to [12], [8] and [9]. Example of one of the two cases S3 at time t_3.

Fluctuating velocities in the x direction are defined such as $u' = u - \overline{U} - u_g$, with $\overline{U}$ the temporal mean velocity and u_g the velocity associated to the grid frequency (resp. $w' = w - \overline{w} - w_g$ in the z direction). We choose to remove u_g to exclude the coherent mechanical stirring of the grid from the definition of the turbulent fluctuations. In our case, this flow represents between 5 and 10% of the turbulent kinetic energy (when defined as $u' = u - \overline{u}$), until a depth of 1.5 M below the grid. It is in agreement with previous observations which found a grid signature until $z' \sim 2M$ below the grid [25]. As a remark, the harmonics of the grid forcing frequency are also present but only really near the grid ($z' < M$). Thus we do not consider them, their contribution being really localized. We also verified that the side borders of the tank influence the flow until $x \sim 1.5M$ from the wall, also in agreement with previous studies [32] (not shown). Therefore, we calculate depth profiles of turbulent quantities by averaging over the x direction excluding 2 M on each side (white rectangle on Fig. 2(b)). In the following $< . >_x$ indicates the average in the x-direction. An example of the depth profile of the horizontal RMS velocity, $U_{rms} = (\overline{u'^2})^{1/2}$ is shown in Fig. 2(c). For each stirring, 300 grid periods are recorded to ensure the statistical convergence of the data for both the mean field and the fluctuating one (not shown here).

III. CHARACTERIZATION OF OGT IN HOMOGENEOUS FLUID

In this section, we discuss OGT in a homogeneous fluid, and especially we describe our approach to determine the eddy viscosity, ν_t, taking into account the turbulence decay. Results are discussed in details for the specific case H12 ($Re_g = 800$) but the same trends are observed for all the cases. The evolution of parameters with the forcing are based on all observations. In Appendix A, the case H3 at high Reynolds number ($Re_g = 7980$) is presented for the two illuminated planes. As a remark related to the discussion on the origin of the vertical coordinate in the introduction, we stress here that we verified that taking z_v or the mean position of the grid has not a significant impact on the exponents of the power law studied in this section.

A. Mean flow

In OGT, due to the finite size of the tank, mean flows can develop [29]. We verify that the flow is essentially controlled by the turbulence by comparing the TKE with the kinetic energy based on the mean flow, K. They are defined for our experimental data respectively as $k = U_{rms}^2 + 0.5W_{rms}^2$ and $K = \overline{u}^2 + 0.5\overline{w}^2$. On the one hand, we verify that $< k/K >_x$ is larger than 1 (Fig. 3(a)); one the other hand, we also verify that turbulence is homogeneous in the $x-$direction (Fig. 3(b)). All the cases presented in the following fulfill these conditions.

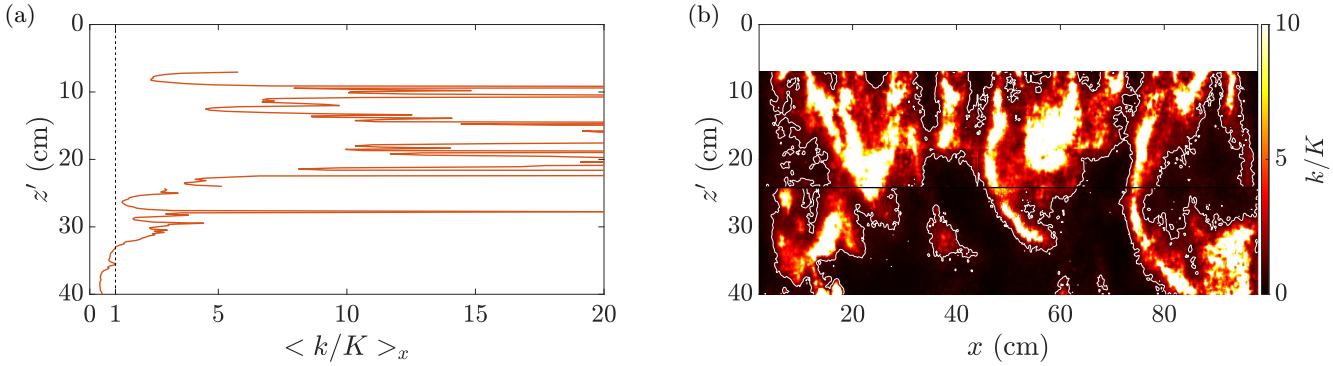

FIG. 3. Example for H12 of : (a) Depth profile of the turbulent kinetic energy, k, over the kinetic energy based on the mean flow, K. (b) Map of k/K to ensure that the turbulence is homogeneous. The white contour line represents $k = K$.

For some stirrings, especially in setup 2, it can be obtained by limiting the depths for data analysis with a cut-off applied at the altitude for which $< k/K >_x = 1$. The summary of all the situations encountered is presented in the last column of Table I.

B. Turbulent properties

We first investigate the RMS velocities, as shown in Fig. 4(a). The vertical profiles are in reasonably good agreement with the first model presented in eq. (1), although a better agreement is obtained with the law proposed by de Silva and Fernando [9] , with $C_1 = 0.25$ and $C_2 = 0.27$ for U_{rms} (not shown) and W_{rms}. Indeed, their law is closer to the analytical solution compared to the others as it was shown by Matsunaga *et al.* [10]. If one wants to compare the profiles to eq. (3), where k is proportional to $(z/L_{\epsilon-k} + 1)^{-5}$, consequently we must consider U_{rms} and W_{rms} to be proportional to $(z/L_{\epsilon-k} + 1)^{-5/2}$. This power law, never tested before on the velocity profiles, is in really good agreement with our experimental data, both just under the grid and far from it where the turbulence decays. As a remark the isotropy is discussed further (see Section IV B) but it is in good agreement with the literature [8] with $U_{rms}/W_{rms} \approx 0.8$.

For the turbulent kinetic energy, observations show a similar agreement with the literature in Fig. 4(b). At intermediate depths, where the turbulence intensity is large enough and not too close to the grid, k is in agreement with the power law z^{-2}. However, as observed for the RMS velocities, a power law of the type $(z/L_{\epsilon-k} + 1)^{-5}$ better describes the profile for k over the entire water column. The fitting parameter k_0 obtained experimentally is in reasonable agreement (about 6 % in average) with the model in eq. (4) (inserted plot Fig. 4(b)). We are also in good agreement with Rastello *et al.* (about 10 % in average, not shown here). Indeed, we are in a range where the two models have

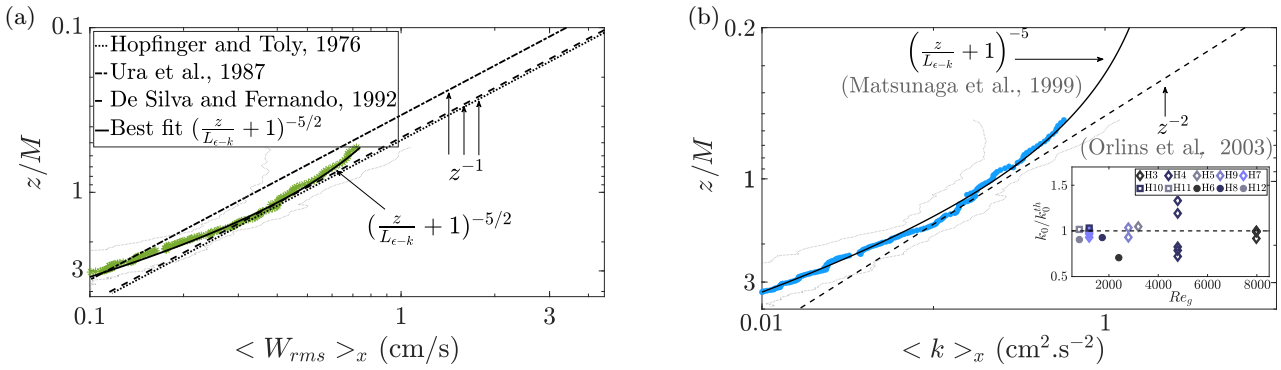

FIG. 4. Depth profiles of (a) the vertical RMS velocity W_{rms} and (b) the turbulent kinetic energy, k. Symbols represent experimental data, with thin lines indicating the uncertainty in the values based on rms variations in W_{rms}/k. Black dashed lines represent the models in eq. (1) or (2) with different values for the constants C_1 and C_2 associated to references, the solid black lines are best fit for a profile coherent with eq. (3) based on experimental data. Inset plot in (b): comparison of the values for k_0 obtained experimentally with its theoretical expression in eq. (4).

similar predictions. As a remark, the estimation of k_0 from fitting the TKE or the RMS velocities (in this case $k_0 = U_0^2 + 0.5W_0^2$) leads to similar values, with a difference of about 10 %.

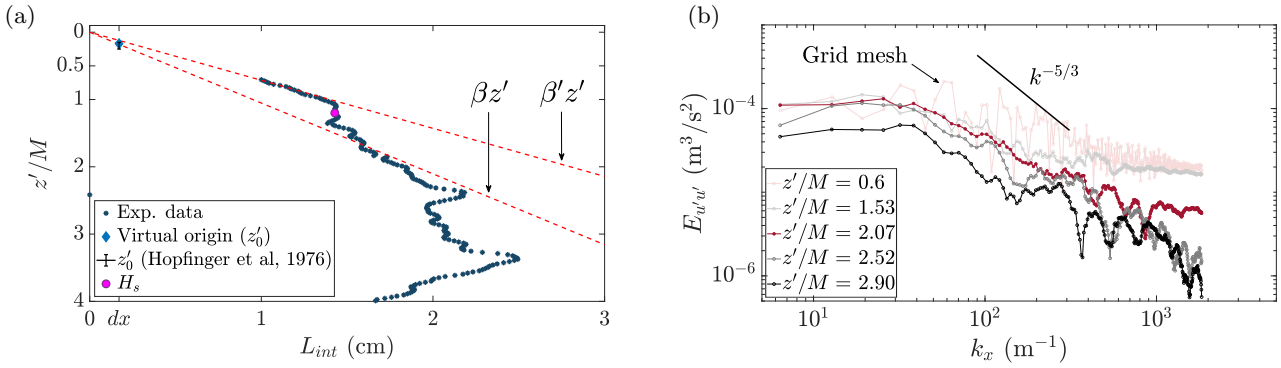

FIG. 5. (a) Depth profile of the integral length-scale, L_{int}. The blue diamond is the virtual origin from the experimental data, found when $L_{int} = dx$, the spatial resolution. The error-bar is the virtual origin from Hopfinger and Toly. Red dash lines are eq. (6) for two proportionality constants. H_s is the depth at which the discontinuity occurs. (b) One dimensional energy spectra of u' for 5 vertical locations.

We now discuss the evolution of the integral length-scale L_{int}. We calculate it from the auto-correlation function of u' in the x direction [33, 34], to obtain its evolution with depth as shown in Fig. 5(a). L_{int} is close to the width of the grid bar, in agreement with previous works [6–9, 30, 35]. The empirical law in eq. (6) is verified and allows us to estimate the proportionality constant β. We find two values for it, one near the grid and one in the region classically studied in OGT where the turbulence is considered homogeneous. Values of β are equal to 0.14 and 0.1 respectively, in agreement with previous studies mentioned before. No trend of β with Re_g is observed (not shown here). We define H_s as the altitude at which the discontinuity occurs (Fig. 5(a)). This specific height is discussed with respect to the turbulence intensity in §III.C, but it has already been observed in previous work [13]. This discontinuity is certainly due to the presence of jets under each grid bar to almost one mesh below the grid (Appendix C). These coherent structures, observed in all cases in homogeneous fluid, have already been mentioned by McCorquodale and Munro [32].L_{int} obtained from the vertical fluctuating velocity has been calculated as well and shows the same tendency with z' (not shown here). We calculate it from the auto-correlation function of w' in the -direction. Since the auto-correlation of w' in the x direction is always smaller than the auto-correlation of u' in the x direction, the integral lengthscale of w' is smaller than that of u', especially near the grid, in agreement with the literature [13, 35]. Finally, the virtual origin, z_v, is estimated by extrapolating $L_{int}(z)$ up to the depth where it equals zero (at the limit of the spatial resolution for PIV). As a remark, we use the extrapolation far from the grid to compare our virtual origin with the literature (i.e. $L_{int} = \beta' z' + z_v$). We found z_v in agreement with the expression $z_v = S/2 + 1 \pm 0.5$ cm proposed by Hopfinger and Toly [8] (errobar in Fig. 5(a)).

When comparing the results for L_{int} with the energy wavenumber spectrum in Fig. 5(b), defined as the Fourier transform of the spatial correlation of the velocity fluctuations [34], this confirms that the quantification of the largest scales of the turbulence from a correlation analysis is a rigorous approach. Indeed, we indicate the length-scale associated with the mesh size which corresponds to a peak in the spectrum near the grid ($z/M = 0.6$), thus the largest eddies of the turbulence are strongly influenced by the grid characteristics (mesh and bar size) [35]. One can observe that the inertial range characterized by the power law $k_x^{-5/3}$ [33], is only observed over one decade due to two specific reasons, the low values of Re_g implying a low intensity of turbulence, and our spatial resolution (≈ 1.5 mm) which is insufficient to resolve the Kolmogorov scale (< 1 mm) (Fig. 5(b)).

We now investigate the dissipation rate, ϵ, and first discuss the best way to estimate it over the entire water column. As presented in Fig. 6, we consider five alternative methods. For more details on each definition of dissipation rate, the reader may refer to Appendix B. A first method to calculate the dissipation rate is to use its definition from the velocity gradients in the three directions (x, y, z). However, using PIV 2D-2C, only two velocity components are accessible. A classical way to overcome this, it is to assume global isotropy (*Isotropy* in Fig. 6) or at least local isotropy (*Local isotropy* in Fig. 6) [30, 36–38]. Nevertheless, at depths between 0 and 2 M below the grid, there is a strong signature of the grid geometry, thus the flow is not isotropic [8, 13, 14, 32]. Furthermore, our spatial resolution is insufficient to solve the Kolmogorov scale (Fig. 5(b)). Therefore, we consider the values of ϵ based on these assumptions on velocity gradients to under-estimate true values near the grid (red and green dotted lines in Fig. 6). The dissipation rate can also be obtained from the energy spectrum. However this technique, based on the estimation of the slope of the energy spectrum in the inertial range, requires data covering at least two decades [10, 38]. In our case, the inertial range is only observed over one decade due to low Re_g, being low turbulence intensity (Fig. 5(b)), and we cannot consider the method. Another approach estimates ϵ from the longitudinal structure function (*structure function* in Fig. 6) based on the first and second Kolmogorov similarity hypothesis [33, 38]. However, even if this technique requires no assumptions on velocity gradients, it does assume 'isotropy'. As stated before, especially under the grid, this leads to under-estimated values of the dissipation (pink dotted line in Fig. 6). Finally, ϵ can be calculated from characteristic length-scales, the integral length-scale [8, 16, 33] and the Taylor scale, λ [34], as shown in black solid line and blue dash-dotted line in Fig. 6 respectively. As a remark, the calculation based on the Taylor scale is also based on the assumption of global isotropy, that is why we exclude the definition of ϵ based on the Taylor scale. A last method to obtain ϵ from TKE and/or L_{int} is discussed in details below. Matsunaga *et al.* mentioned that for OGT, $\epsilon(z')$ and

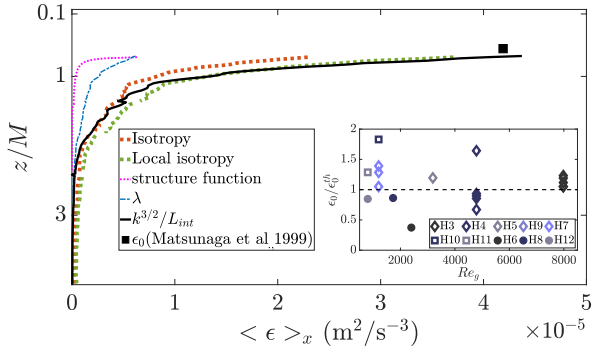

FIG. 6. Vertical profiles of the dissipation rate calculated from five definitions with different assumptions. Inset plot : comparison of ϵ_0 obtained experimentally with its theoretical expression in eq. (4) [10].

$k(z')$ are related but that the definition $\epsilon = k^{3/2}/L_{int}$ is not obvious if L_{int} is a linear function with z' and $k \propto z'^{-2}$. Actually, the authors defined $L_{int} = k^{3/2}/\epsilon$ and found that $L_{int} \propto z'$ while $\epsilon \propto k^{1.7}$ from several experiments [10], that are reproduced in Fig. 7(a). We compare their observations with all our runs, with the values of ϵ computed from the local isotropy assumption. Indeed, this definition is acceptable far away from the grid, and we extract data only from depths z' larger than $1.5M$ to avoid under-estimations. One can notice that a clear trend with k appears (Fig. 7(a)), which is best described by a power law $\epsilon \propto k^{1.3}$ as indicated by a thin black line. Our results cover a larger range of values than those obtained by Matsunaga *et al.*, which we did find to increase slightly faster with $k^{1.6}$ (not 1.7 actually), as indicated by a dashed black line. When comparing the values of TKE and energy dissipation rescaled by the predicted values at the grid (k_0 and ϵ_0), as shown in the insert of Fig. 7(a), there is a greater scatter of the results, nevertheless the differences between the two dataset are less obvious and both power laws could then be valid. It is worth noting that in the work of Matsunaga *et al.*, since $k \propto z'^{-5}$ and $\epsilon \propto z'^{-8.5}$, then $L_{int} \propto z'$. In our case, we can thus consider that the values of L_{int} and k can predict ϵ, since they are in agreement with the results in [10]; it is tested in Fig. 7(b). Some discrepancies are visible when turbulence is weak ($\epsilon < 10^{-6}$ m^2/s^3), or for large

values ($\epsilon > 10^{-4}$ m^2/s^3) but that might be underestimated as discussed before.

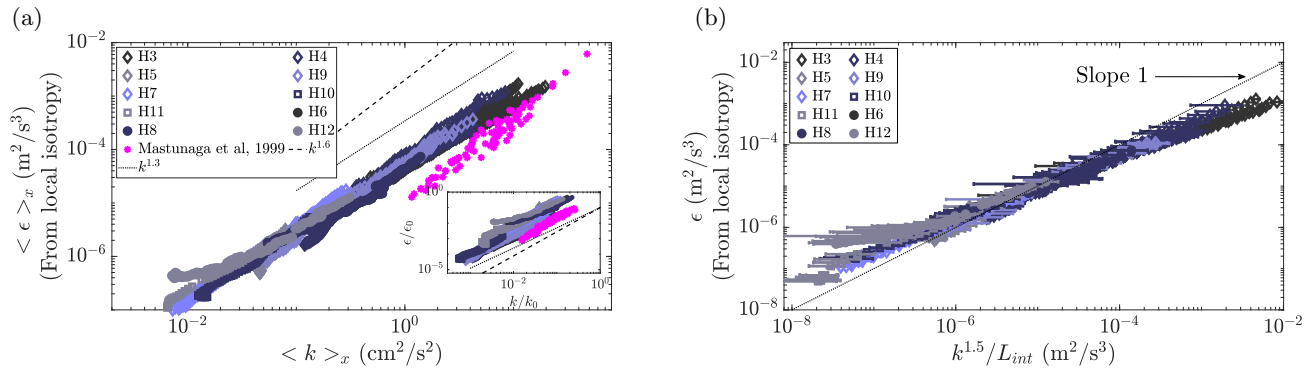

FIG. 7. (a) Dissipation rate, ε, from local isotropy assumption as a function of the turbulent kinetic energy, k for all our runs. The data of Matsunaga *et al.* are also added [10]. The inset plot represents the same graph considering the normalized quantities. (b) Comparison between ϵ from local isotropy assumption and from k and the integral length-scale.

To conclude, we consider ϵ based on the definition with L_{int} as the best approach for our measurements. Its value at $z' = S + d_b$ is in reasonable agreement with the value ϵ_0 provided by Matsunaga *et al.* [10] (black square in Fig. 6). Comparison of all the values of ϵ_0 obtained experimentally ($\epsilon_0 = 1.82 k_0^{1.5}/L_{\epsilon-k}$) with the model in eq. (4) are shown in the inserted plot in Fig. 6. An higher discrepancy than for k_0 is observed with a difference of approximately 18 %, with the theoretical expression in eq. (4) and about 22 % with Rastello *et al.* [11] (not shown here). It is probably due to the addition of the uncertainties for both k_0 and $L_{\epsilon-k}$. We checked that the origin of z (mean position of the grid or z_v) does not affect either the discrepancy or the values of k_0 and ϵ_0 (not shown here).

C. Turbulent eddy diffusivity

We conclude this characterization of the turbulence by computing the eddy viscosity ν_t, using the $k-\epsilon$ model with the definition of $\epsilon = k^{3/2}/L_{int}$. In this context, we can write

$$\nu_t = 0.09 k^2/\epsilon = 0.09\sqrt{k} L_{int}\,. \tag{8}$$

The corresponding vertical profile of ν_t is presented in Fig. 8(a) and compared to three models defined below. The first two models are obtained by substituting eq. (2) and (6) into eq. (8) for ν_t^P, and by substituting eq. (3) and (6) into eq. (8) for ν_t^M, leading to

$$\nu_t^P = 0.09\,\beta\,(C_1^2 + 0.5\,C_2^2)\,\sqrt{M}\,S^{3/2}\,f_g\,, \tag{9}$$

$$\nu_t^M = 0.09\,k_0^{1/2}\beta\,z\left(\frac{z}{L_{\epsilon-k}} + 1\right)^{-5/2}\,. \tag{10}$$

Both models give the opportunity to predict the eddy viscosity profile, if we use the value for β measured near the grid (Fig. 5(a)). We verified that for all stirrings, ν_t^P is a good approximation for the eddy viscosity near the grid, over a certain depth H_s (Fig. 8(b)). However, it does not catch the turbulence decay unlike ν_t^M which qualitatively catches it. Nevertheless, ν_t^M under-estimates the eddy viscosity near the grid and over-estimates it far from the grid. This is partly explained by the variability in β.

As a better fit for the experimental observations, we propose a simplified model ν_t^S, which combines features from both ν_t^P and ν_t^M,

$$\nu_t^S = \begin{cases} \nu_t^P & \text{if } z < H_s, \\ \alpha\, z^{-3/2} & \text{if } z > H_s. \end{cases} \tag{11}$$

where α and H_s are adjusted for each experiment. Here we have simplified the power-law in z for depth larger than H_s since for all cases, we verified that $H_s/L_{\epsilon-k}$ is always much greater than 1 (between 50 and 200 typically). This pragmatic model is shown in Fig. 8(a) with the dotted curve. It seems to better describe the behaviour of ν_t and especially its decay. One of the major knowledge gap in the description of ν_t^S is value for H_s. We remind that H_s corresponds to the height at which the discontinuity of L_{int} occurs (Fig. 5(a)). It seems to be a good cutoff scale for

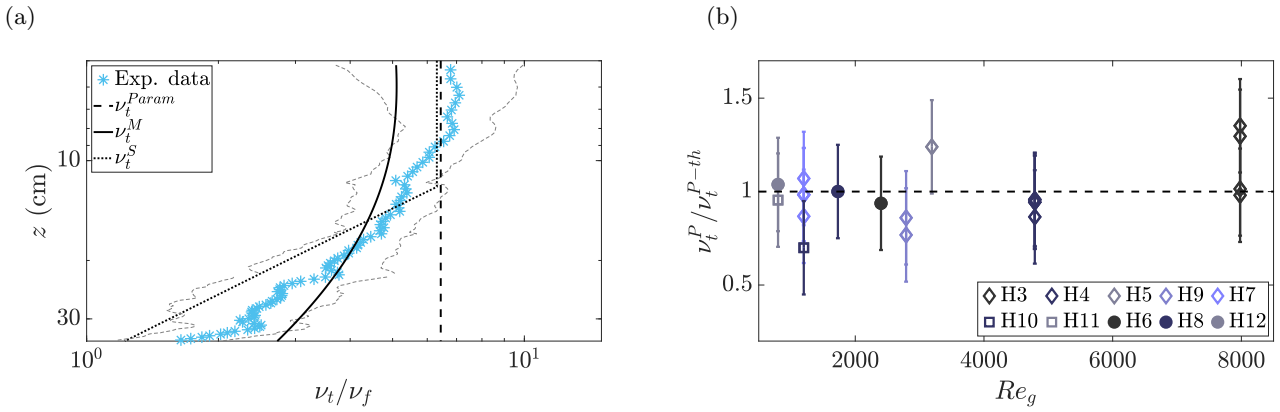

FIG. 8. (a) Depth profile of the eddy viscosity, ν_t, normalized by the fluid kinematic viscosity ν_f. Symbols are experimental data with thin blue lines indicating the uncertainty in the values. Black lines are the parametric laws from equations (9) to (11). (b) Comparison of ν_t^P as mean value of experimental ν_t over H_s and the theoretical expression eq. (8), ν_t^{P-th}.

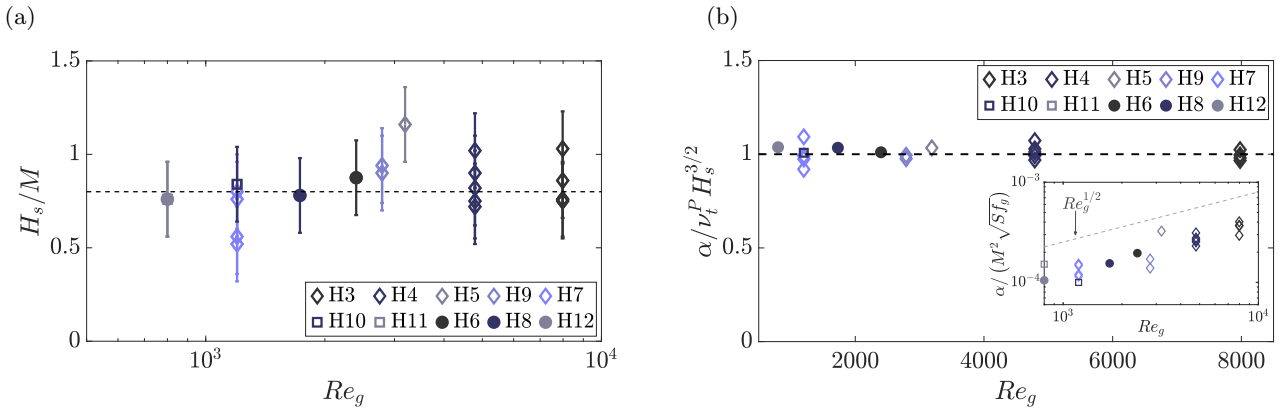

FIG. 9. (a) Evolution of H_s, the depth over which the eddy viscosity is almost constant, as a function of the grid Reynolds number, Re_g. Here H_s is express as the distance under the grid. (b) Evolution of α, the proportionality constant of ν_t^S when $z > H_s$, as a function of the Reynolds number.

the eddy viscosity. Indeed, estimating H_s directly from $\nu_t(z)$ (not shown here) leads to similar values of H_s estimated from the integral length scale. Even if a more complete dataset is needed, no grid Reynolds number dependence appears for H_s with

$$H_s \simeq 0.8\, M \tag{12}$$

under the grid (Fig. 9(a)). By evaluating eq. (11) at $z = H_s$, we can deduce the expression for α

$$\alpha = \nu_t^P H_s^{3/2}. \tag{13}$$

It is well verified experimentally (Fig. 9(b)). As a remark, a dependence with M, S, f_g and Re_g is observed (inserted plot Fig. 9(b)). Once again, it is a good agreement with the dependence expected. Indeed, from eq. (9) and from eq. (12) we deduce that $\nu_t^P \propto (MSf_g\, Re_g)^{1/2}$ and $H_s \propto M$. Consequently from eq. (13), α should be proportional to $M^2(Sf_gRe_g)^{1/2}$, what we found experimentally (inserted plot Fig. 9(b)). To our knowledge, there is no data in the literature, measuring the eddy viscosity in grid turbulence, to compare with this approach, that we summarize as eq. (11), eq. (12) and eq. (13) .

IV. CHARACTERIZATION OF OGT IN TWO-LAYER FLUIDS

We now investigate OGT in the case of a two-layer fluid, and especially we compare it with its counterpart in homogeneous fluid. The major difference is the presence of the interface which acts as a barrier at a certain depth for

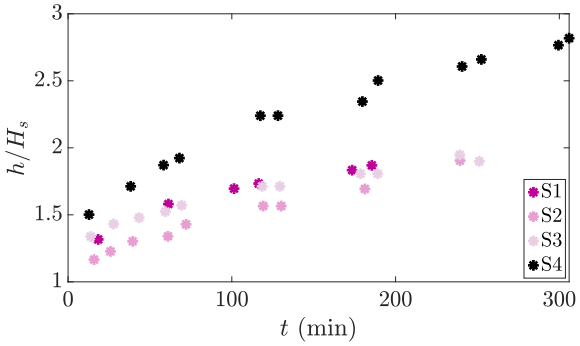

FIG. 10. Time evolution of the position of the interface, h, normalized by the depth H_s over which the eddy viscosity is almost constant.

the turbulence. The depth of the interface slowly moves away from the grid with time as mixing occurs. For each case, the position of the interface is initially further than the distance H_s from the grid as shown in Fig. 10. As a remark, the distance H_s is deduced from eq. (12). For the comparison of profiles at various times, we will use the vertical coordinate as well as a non-dimensional coordinate using the position of the interface h for the two-layer fluid, and H_s for the homogeneous one to rescale the z-axis. For each value of Re_g, the instants at which the turbulent properties are computed are labelled t_i, with $2 \leq i \leq 8$. Each PIV measurement is associated with two density profiles recorded by the conductivity and temperature probe. Only the two first instants are associated with one density profile because of experimental constraints (Fig. 10).

A. Mean and coherent flows

In the two-layer case, we ensure again that the turbulent intensity is higher than the mean flow in the upper layer (not shown). We remind that the interface acts as a barrier (no motion below the interface is observed), thus in the following we only discuss the flow for $0 < z < h$. For all cases, the mean flow is stronger than in the homogeneous case as illustrated for the case of S3 in Fig. 11. Near the interface, regular patterns are observed (Fig. 11(b,e)). These patterns persist over time (Fig. 11(c,f)) and they are systematically present for all stirrings. Between experiments, the only difference is the number of patterns which varies between 2 and 4 depending on f_g, but we do not explain this dependence. We can notice that these patterns are the signature of the transfer from vertical scales to horizontal ones.

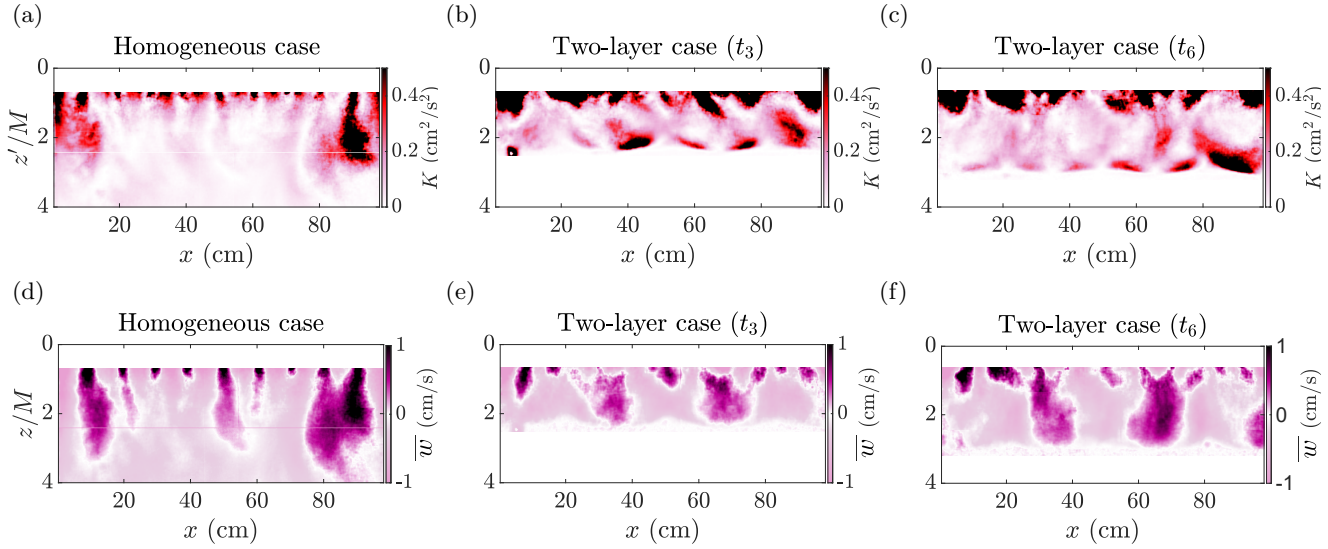

FIG. 11. Examples of maps of the mean kinetic energy K (top) and vertical velocity $\overline{w}$ (bottom), in (a,d) homogeneous fluid (case H12) and (b,c,e,f) two-layer fluid at two different times (case S3).

Indeed, looking at the vertical mean velocity component, the mean flow seems to be organized in jet-like structures, as observed in Fig. 11(e) and (f). We also note that these structures are different from the ones in homogeneous fluid (Fig. 11(d)). Indeed, for this case, finer jets are observed under each grid bar and vertical flow is dominant near the grid ($z/M < 1.5$ and 20 cm $< x <$ 80 cm) and near the side-walls ($x <$ 20 cm and $x >$ 80 xm).

We also investigated the presence of internal waves in the velocity data, especially near the interface, and more details are presented in appendix D. A weak signature of internal waves dynamics is visible in the density spectrum of both the horizontal and vertical velocity components, for depths between $0.8h$ and h. Overall, the energy of the signal for internal waves is small compared to the one related to turbulence above the interface ($z/h \leq 0.6$).

B. Overall turbulent properties (far from the position of the interface)

First, we discuss the turbulent properties far from the position of the interface. We focus on what happens at the vicinity of the interface in Section IV C.

We start the discussion with the loss of isotropy near the position of the interface (Fig. 12(a)). Indeed, U_{rms}/W_{rms} is no longer constant in the vicinity of h, unlike the case in homogeneous fluid. This phenomenon, well known in the literature, corresponds to the energy transfer from vertical to horizontal scales [8, 20, 23]. From our experimental data, it seems that the loss of isotropy appears after a depth of 0.6 to 0.8 h. Thus, the interface can affect the flow over a significant depth above it. One can also notice in Fig. 12(a) that the maximum value for U_{rms}/W_{rms} is always reached at a depth, $z_{Max\ Iso}$, smaller than h (indicated by horizontal dash lines). We discuss more in details where it occurs in the next section, this can be related to the mixing processes that take place in the upper layer only [18, 23].

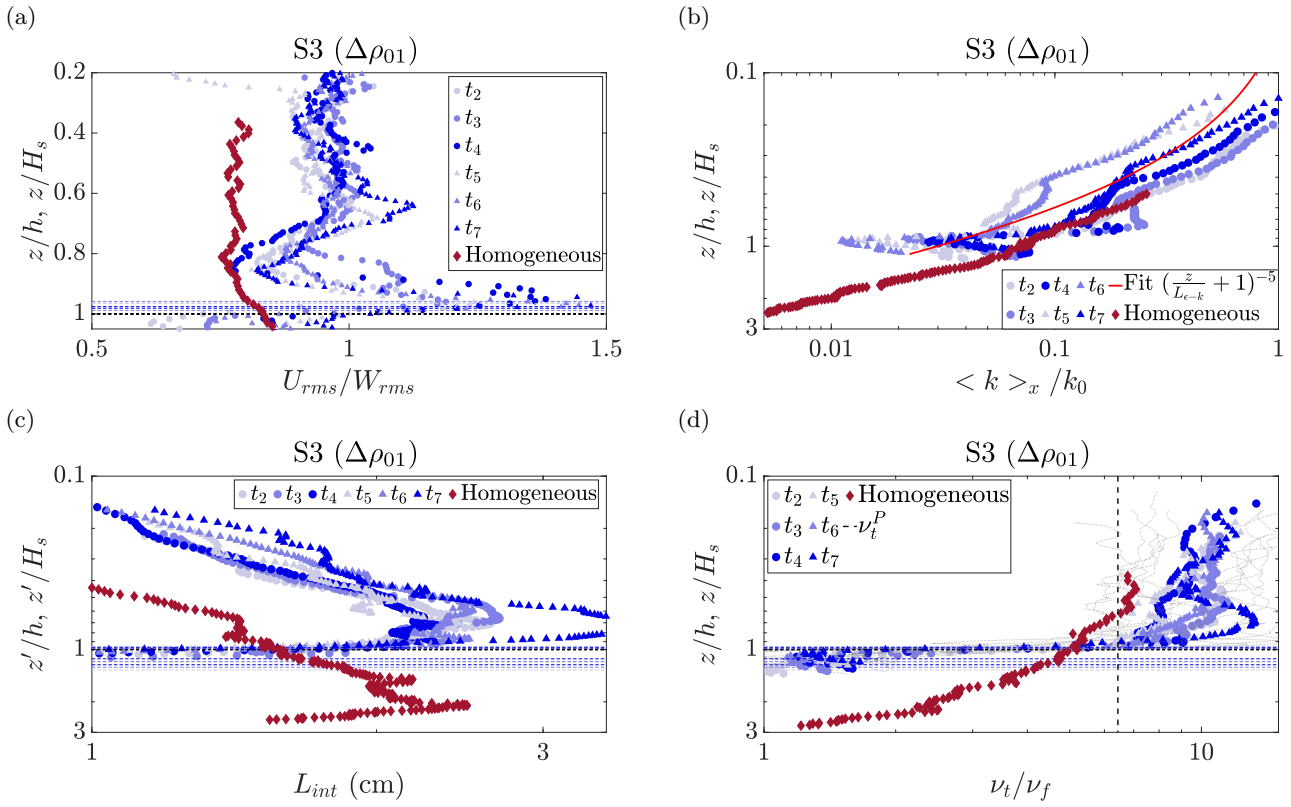

FIG. 12. Depth profiles of (a) the isotropy degree, (b) TKE, (c) integral length-scale, and (d) turbulent eddy diffusivity, with the z-axis starting from the top position of the grid normalized by h for the two-layer fluid and by H_s for the homogeneous fluid; for case S3 ($\Delta\rho_1$).

We now look at the turbulent kinetic energy profiles in Fig. 12(b). If we focus more on the upper part of the fluid (near the grid), there is not a big difference between homogeneous and two-layer cases for depths smaller than $0.6h$ (also true without the normalization of the z-axis). The parameters estimates from the homogeneous models, such as eq. (4), can be estimated by fitting the profiles over $[0, 0.6h]$, and their evolution with time is shown in Fig. 13(a).

Except at large times when the TKE no longer decreases like in the homogeneous case and thus k_0 (through $L_{\epsilon-k}$) is

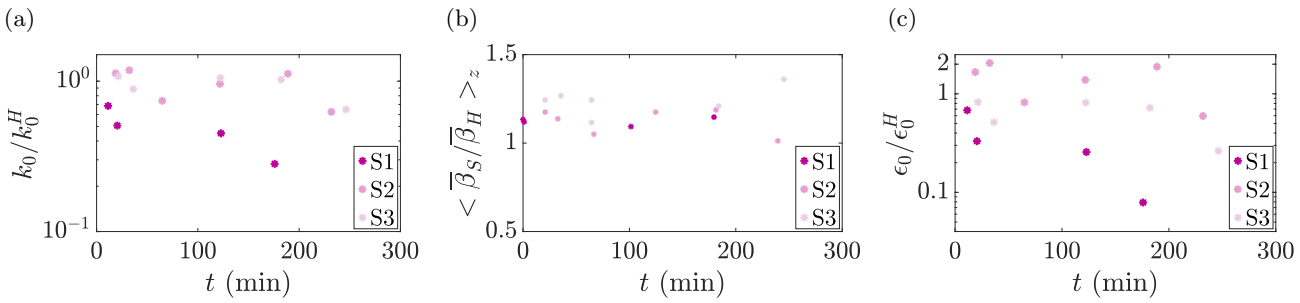

FIG. 13. Temporal evolution of (a) k_0 normalized by the k_0^H measured experimentally in homogeneous fluid, and (b) the proportionality constant β_S, for the integral length scale from eq. (6), normalized by the proportionality constant in homogeneous fluid β_H, (c) ϵ_0 normalized by the ϵ_0^H measured experimentally in homogeneous fluid.

affected (Fig. 12(b)), the values for the parameters are quite constant, with k_0/k_0^H of the order of 0.80 ± 0.22.

Similarly, we can study the integral length-scale profiles in Fig. 12(c), and discuss its shape with time and with two specific regions of interest. At first, a general comment is that L_{int} is still of the order of the grid bars, at a fixed depth the integral length scale is generally larger in the two-layer fluid than in the homogeneous case (the difference between the two near the grid is small if one compares non-stretched profiles). Second, L_{int} no longer appears as a piece-wise function with a clear discontinuity as in the homogeneous case. This could be explained by a different flow under the grid in the case of a two-layer fluid, as detailed in the Appendix C. Indeed, in the stratified case, the jets under the grid bars disappear and larger structures appear up to 1.5 M under the grid. Finally, a clear difference appears with a strong peak for L_{int} before it tends to zero when it reaches the interface. We will see in the next section that the peak value of L_{int} plays a key role in the description of the turbulent quantities in two-layer fluid.

Finally, from the two quantities studied, k and L_{int}, one can combine them to compute the dissipation rate and the eddy viscosity, shown in Fig. 12(d). The evolution of ϵ_0/ϵ_0^H is shown in Fig. 13 (c). Like in homogeneous fluid, due to the addition of uncertainties of k_0 and $L_{\epsilon-k}$, an higher discrepancy than for k_0 is observed. From our data ϵ_0/ϵ_0^H is quite constant and of the order of 0.9 ± 0.6. From our data, it is difficult to conclude about quantitative difference between OGT in two-layer fluids and in homogeneous fluids in the upper part of the fluid, far enough from the interface. However, we observe a clear difference in the profiles near the interface. Nevertheless, in the two-layer fluid, ν_t turns out to be almost constant with z, before it sharply decreases to ν_f at the vicinity of the interface. This is quite surprising since in the homogeneous fluid ν_t is almost constant over a certain depth, H_s, before decreasing with power law $z^{-3/2}$. As already mentioned, our experiments are with $h > H_s$ (Fig. 10) at all time hence the decay should have been observed if existing. We can thus conclude that in the two-layer case, the turbulence decay over depth is cancelled or at least put off by the presence of the interface until $h > 2H_s$, although this bound shall be investigated in a specific study. It could be explained by the simultaneous increase of TKE and L_{int} near the position of the interface due to the confinement of the energy in the upper layer. It is also interesting to note that the temporal variability observed regarding the eddy viscosity is weak (Fig. 12(d)), suggesting that describing OGT using ν_t instead of TKE, as it is usually done, can be a simpler approach. For the highest stirrings ($Re_g = 2400$ and $Re_g = 1730$), the parametric law ν_t^P from homogeneous fluid is a good approximation for ν_t (see Fig. 25 in appendix E). However, for the lowest ones ($Re_g = 800$ and $Re_g = 590$), it leads to under-estimations of about 35 % the eddy viscosity (Fig. 12(d)). It could be of interest to investigate in more details the reasons for this discrepancy in ν_t^P, More experiments on a larger range of Reynolds number have to be performed to confirm it.

C. Turbulent properties near the interface

We now look at turbulent quantities at the vicinity of the interface ($0.6 < z/h < 1$). We discuss how the loss of isotropy and the increase of both TKE and L_{int} occur linked to the flow scales. In the following, we will preferentially use the peak value of the integral length-scale, that we note L_{int}^{max}, as a reference length-scale. Comparing L_{int}^{max} with the integral length-scale at the the position of the interface in homogeneous fluid, L_{int}^H, we find from our experimental data that $L_{int}^{max} = 0.9\, L_{int}^H$ (not shown). It is in agreement with results obtained near a solid boundary [39]. Moreover, as illustrated in Fig. 14(a) for case S3, the decrease of L_{int} occurs at $(z' - h) \simeq L_{int}^{max}$ to reach $0.6\, L_{int}^{max}$ at $(z' - h) = 0$, like in OGT near a solid boundary [39]. As a remark, we also compared the peak of the integral length-scale with the interface thickness, δh, but no clear correlation was observed (see section V).

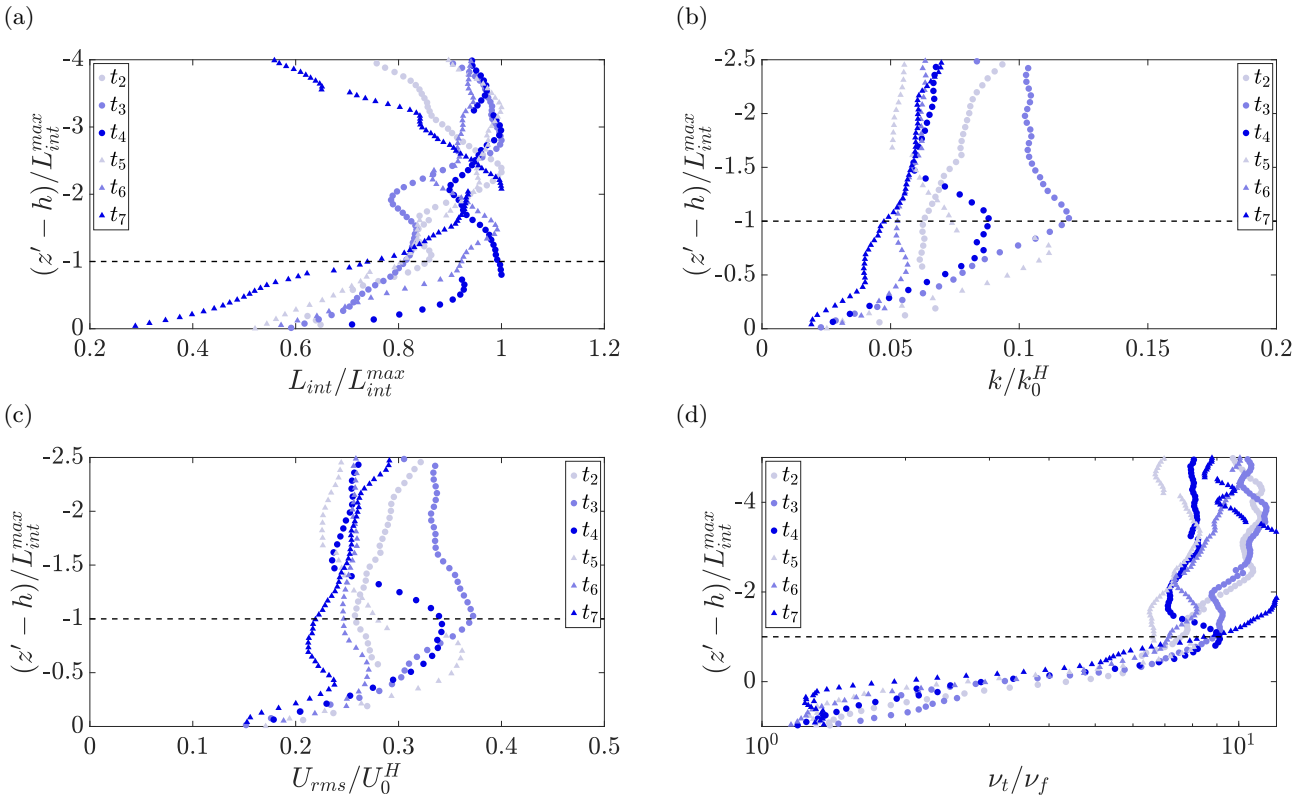

FIG. 14. Depth profiles of (a) L_{int}, (b) TKE, (c) RMS horizontal velocity normalized by the same quantity at $z = h$ in the homogeneous fluid case, and (d) the eddy viscosity normalized by the kinematic viscosity of the fluid. The vertical axis now starts from the position of the interface, h, and is normalized by L_{int}^{max}. Zoom on case S3 ($\Delta\rho_1$) in the region $0.6 < z/h < 1$.

If we look at the distance from h where the loss of isotropy occurs (Fig. 12(a)), it seems that the location of the peak of anisotropy evolves slowly with time. At early times ($t < 60$ min), it occurs at $0.7\,(\pm 0.3)\,L_{int}^{max}$ above h while at large times ($t > 60$ min), except for $Re_g = 1730$, it occurs at $0.4\,(\pm 0.2)\,L_{int}^{max}$ above h. We do not clearly understand this decrease. Despite this, on average over all times, we found that the peak of anisotropy occurs at $0.55\,(\pm 0.25)\,L_{int}^{max}$ above h. It is again in reasonable agreement with results near a solid boundary [39], where the peak occurs between $0.7\,L_{int}^{max}$ and L_{int}^{max} above the plate. Our data are also in good agreement with a study of OGT in two-layer fluid [23], which uses the integral length-scale at $z = h$ in homogeneous fluid instead, and found $z_{Max\ Iso}$ close to $0.6\,L_{int}^{H}$ above h [23]. Regardless the definition of the integral length-scale, we observe that the transfer from vertical to horizontal scale occurs always from the position of the interface (in the upper layer). More precisely it occurs at about 0.6 integral length-scale above the position of the interface. It confirms that the the mixing processes that take place in the upper layer only [18, 23].

Similarly we can study the TKE in the region $0.6 < z/h < 1$, where a peak is observed. There is a strong temporal variability, with a loss that can reach 20 % of the initial TKE in 3 h for some cases (S2, not shown). To highlight this aspect, the z-axis is rescaled with respect to the integral length-scale as well (Fig. 14(b)). At early times (t_2 and t_3), when the steady state is not necessarily reached, there is an increase of the TKE at $(z - h) = L_{int}$. At later times ($t_i > t_3$), the peak appears at $(z - h) \approx 0.5\,L_{int}$. It is in reasonable agreement with results in two-layer fluid [23] and near a solid boundary [39] who found a maximum of TKE at $(z - h) \approx 0.3\,L_{int}$. The peak of TKE is linked with the transfer from the vertical to the horizontal scales. More precisely, it is due to the local increase of U_{rms} as shown in Fig. 14(c), with the peak value of the horizontal fluctuating velocity having a similar evolution than the TKE. The variation of the peak intensity is consistent with the fact that the energy that would diffuse in the rest of the tank is now trapped in a layer of increasing depth. A classic way to discuss this aspect is to use the vertical flux of TKE, $\overline{k'w'}$ Hannoun *et al.*, McCorquodale and Munro [23, 39]. However, from our experiments this quantity is too noisy to draw some conclusions (not shown).

Finally, we focus on the eddy viscosity at the vicinity of the interface. We observed that ν_t decreases below $z = L_{int}^{max}$ (Fig. 14(d)), with all the curves collapsing in a single trend. At the interface ($z' = h$), the eddy viscosity is really weak ($\nu_t < 3\nu_f$). Once again, it confirms the turbulence is trapped in the upper mixed layer.

D. Synthesis

In conclusion, in the region $0 < z/h < 0.6$, no significant difference of the turbulent quantities between the OGT in homogeneous or two-layer fluid is observed. On contrary near the position of the interface, in the region $0.6 < z/h < 1$, there is a loss of the isotropy and a clear increase of values for TKE and L_{int} compared to the homogeneous case, which results in a nearly constant value of ν_t with depth. These differences are due to (1) the transfer from the vertical scales to the horizontal ones and (2) the confinement of the TKE in the upper layer, both induced by the presence of this deformable interface. Similar observations have been obtained previously in OGT studies with a two-layer fluid or near a solid boundary [23, 39], where they identified that the isotropy and the maximum increase of the turbulent quantities occur about one integral length-scale above the boundary (interface or rigid plate).

Overall, in terms of the description of the eddy viscosity, we observed that ν_t is nearly constant over the range $0 < z/ < h - L_{int}^{max}$, and sharply decreases to ν_f over the distance of one integral length scale. The parametric model ν_t^P in eq. (9) can be used for the estimate over the entire depth h (although $h/H_s > 1$), with a tendency to underestimate (about 35%) the observed values at Re_g smaller than 1700.

V. MIXING

The mixing is related to the spatial evolution of the interface. It is well-known that in the setup considered here, the thickness of the interface and the density difference evolve with time [3, 18]. In order to fix the position of the interface, some authors used two oscillating grids on each side of the interface [19]. Others tried to keep a constant density difference, $\Delta\rho$, between the two fluid layers, adding fresh water in the stirred layer [17]. However, in each case the steady sate was not reached. Indeed, to ensure a steady state, both the position of the interface and the density difference have to remain constant as mentioned by Verso *et al.* [16], who proposed an interesting model based on the flux balance to characterize the entrainment and thus the mixing. To apply it, a specific setup is needed with inflows and outflows of water. Our setup cannot be transformed with inlets/outlets, consequently both the interface and the density difference evolve with time.

In the section, we investigate the time evolution of the interface depending on the stirring. Then we discuss the nature of the turbulence decay in terms of the entrainment rate. Finally, thanks to our large field measurement we discuss the erosion process in our case of OGT.

A. Position of the interface with time

Previous studies have mainly investigated the mixing in terms of temporal evolution of the interface. Before discussing it in more details, we mention that the variation of h is associated with a variation of ρ_1 such as the quantity $\Delta\rho g h$ is preserved (Fig. 15(a)). Huppert *et al.* [3] proposed the following expression for the position of the

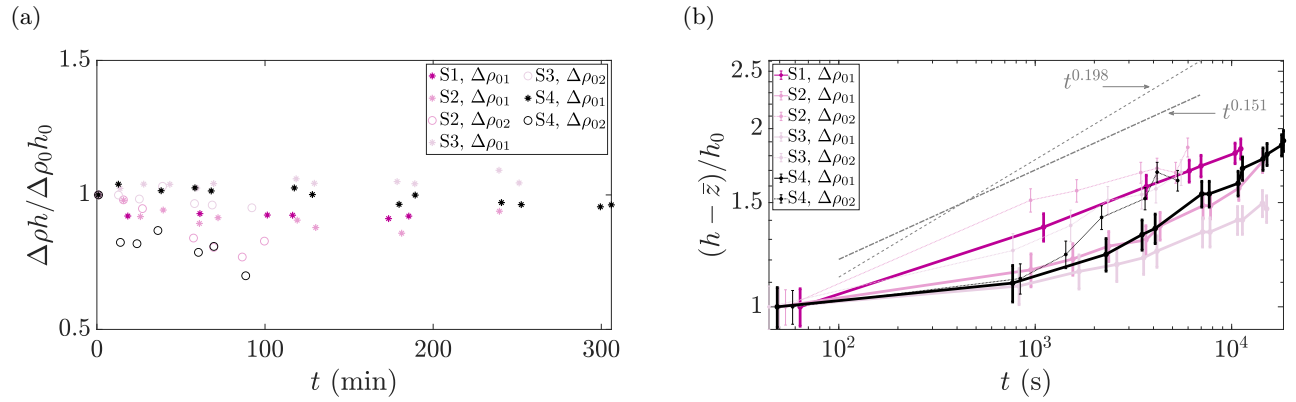

FIG. 15. (a) Time evolution of the density difference, $\Delta\rho$ multiplied by h. This quantity is normalized by its value at the initial time step, $\Delta\rho_0 h_0$. (b) Time evolution of the position of the interface, h, normalized by its initial value h_0. In order to compare with the power law proposed by Huppert *et al.* [3] (dash-dotted line), the mean position of the grid, $\overline{z}$, is subtracted from h.

interface as a function of time

$$h - \overline{z} = Bt^b = C_B \left[\frac{\omega_g^3}{g'h}\right]^b t^b \,, \tag{14}$$

where $\overline{z}$ is the mean position of the grid, $\omega_g = 2\pi f_g$ is the frequency of the grid, $g' = g(\rho_2 - \rho_1)/\rho_1$ is the reduced acceleration due to gravity and b an exponent lower than 1. They found $b = 0.151 \pm 0.008$, constant with $\Delta\rho$ and f_g for a given stroke. Even if we found a higher discrepancy of the power $b = 0.198 \pm 0.056$, our values are in agreement with the one found by Huppert *et al.* [3]. No clear dependency is observed neither with respect to the initial value of $\Delta\rho$ nor Re_g (not shown). The authors did not comment on $C_B = B(g'h)^b/\omega_g^{3b}$, which was a constant in their study. By dimensional analysis, C_B has to be proportional to a length-scale at the power $1 + 2b$. Thus we tried to link C_B with characteristic length scales of our experiments, the stroke and the grid mesh. We tested four possible combinations, presented in Fig. 26 in appendix. The scaling depending only on the stroke leads to a relatively good prediction for C_b with a slight offset (Fig.26 (a)). Combinations of both S and M are also possible for C_B, and data seem closer to the slope 1 when adding the mesh size, as shown in Fig.26(b) to (d). The best agreement is found for the scaling SM^{2b}, for which all data collapse on the slope 1 (Fig.26(d)). Thus the temporal evolution of the position of the interface is best predicted by

$$h - \overline{z} = SM^{2b} \left[\frac{\omega_g^3}{g'h}\right]^b t^b \,. \tag{15}$$

Regarding the time evolution of the interface thickness, δh, we verified that it reaches a steady state, lower than the its initial value (see Fig. 27 in appendix). The nearly-steady value of δh is about $0.1h$, which is in agreement with Fernando and Long [25], and of the same order of the integral length-scale of turbulence at the interface L_{int}^{max}. This indicates that the interface dynamics is controlled by the turbulence, but there could be some more complex equilibrium with molecular diffusion being stronger with a sharp density change [19].

B. Entrainment law

As discussed in the introduction, we seek to characterize the entrainment rate as a function of the Richardson number as in eq. (7). Both quantities are based on turbulent flow properties that we consider in details below. The Richardson number is usually defined as $Ri = g\Delta\rho L_{int}/\rho_1 U_{rms}^2$, with the RMS velocity being the value in a homogeneous fluid, evaluated at the depth of the interface. Our results based on this convention are presented in Fig. 16(a). A power law evolution of E with Ri seems to be a correct validation for each experiment, however there is no clear collapse of the different curves obtained for various values of the frequency and stroke for the grid in setup 1. For $Ri < 1000$, a power law evolution with the power γ being between -1.2 and -1.5 seems to fit with our data. This tendency is in agreement with previous results [15, 26]. For larger Richardson number ($Ri > 1000$), another tendency is observed that tends to flatten. Despite a small number of points for $Ri > 1000$, E seems to tend towards a constant value varying with the initial density difference (black dots on Fig. 16(a)). It must be noted that past results having a clear collapse of their data for mixing always corresponded to a constant stroke or frequency for the grid oscillation, which is not our case here.

We mentioned in the introduction that $U_{rms} \propto z^{-n}$, with past studies discussing the appropriate value for n but always using this parametric law. Using this assumption, the definition of E in eq. (7) and the expression in eq. (14), Huppert *et al.* [3] demonstrated that the choice for n prescribes the exponent in the power law in Richardson number, namely

$$\gamma = \frac{1 - b^{-1}}{2n} - \frac{1}{2}. \tag{16}$$

Based on power law estimates for each case in Fig. 16(a), we can compare the values for γ from our experiments with respect to the theoretical prediction in eq.16, taking $n = 1$ or $n = 5/2$, this latter value having the best agreement with our observations for velocities in Section III B. On average, the evolution of the mixing rate for each experiment is better predicted when $n = 5/2$, although the comparison is not perfect, (mismatch in the exponent of 20% to 60%, not shown), which corresponds to $\gamma = -1.51$ with $b = 0.198$.

Although the exponent in the power law of eq.(7) could be identified, the lack of collapse of the observations onto a single curve with variations of the experimental parameters (grid and fluid) leads us to consider alternative definitions for the relevant turbulent quantities to consider. Indeed, we have shown in §IV C that the turbulence is altered at

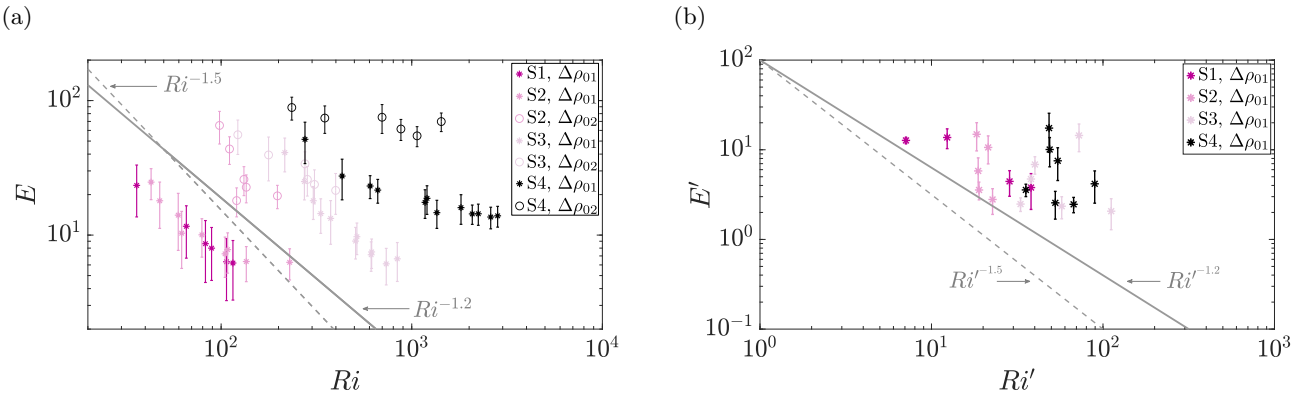

FIG. 16. (a) Entrainment rate, E, as function of the Richardson number, Ri. (b) Entrainment rate based on U_{rms}^{max} as function of the Richardson number, Ri', based on the peak values of U_{rms} and L_{int} near the position of the interface.

the interface, and it can modify the amplitude of the turbulent properties (especially U_{rms}, k and marginally L_{int}) compared to the homogeneous fluid. Thus, we now evaluate the quantities in eq. (7) based on the turbulent properties estimated at one integral scale from the interface (L_{int}^{max}), where we observed a peak of intensity for L_{int} and U_{rms} in the two-layer case. Based on these two values, we define a new Richardson number and a new entrainment rate such as $Ri' = g\Delta\rho L_{int}^{max}/\rho_1 {U_{rms}^{max}}^2$ and $E' = U_e/U_{rms}^{max}$. Our results are presented in Fig. 16(b). As a remark, there are less points than in Fig. 16(a) because we reported only data for which we did PIV measurements. Indeed, we are not able to predict U_{rms}^{max} from homogeneous fluid, this parameter depending on both the stirring and the distance of the grid. On the one hand, using Ri', data better collapse in a more continuous range of values, which is an indication that the use of a Richardson number based on local turbulent flow quantities (U_{rms}^{max} and L_{int}^{max}) could be more appropriated to describe the mixing process. On the other hand, even if, our data are in reasonably agreement with the law in power -1.2, the scattering of the data is now greater and uncertainties on the exponent are important.

C. Remarks on the origin of mixing

Mixing in OGT is thought to be controlled by local and intermittent events associated to scales larger than the turbulence at the interface (supposedly based on internal waves properties) or by small coherent vortical structures [1]. Thanks to the large field of view and spatial resolution in our experiments, we were able to catch both the large scale structures and the turbulent properties and discuss this aspect. The results obtained in the previous section suggest that indeed, the entrainment law can be prescribed by a power law based on the relevant Richardson number, obtained by considering the true scales of the turbulent shear at the interface for a turbulent flow in a two-layer fluid (U_{rms}^{max} and L_{int}^{max}).

Yet, as presented in Section IV A, we have also observed some mean flows in most of the cases studied although the turbulent flow is the dominant feature in terms of kinetic energy ($k \gg K$). These structures observed for the mean flow are very similar to downward jets. Mixing induced by a turbulent jet or plume incident onto a two-layer fluid interface is a very similar topic of research that has also been a challenging problem to identify the mechanisms at stake, as summarized in [40]. The entrainment law is then described based on the characteristic vertical velocity of the plume (or jet) at the interface, w_{jet}, and usually compared to a power law in Froude number $Fr_i = w_{jet}/\sqrt{g' r_{jet}}$ with r_{jet} the radius of the plume (or jet) at the interface and g' the reduced gravity. Although our velocity measurements are in a plane not centered on the multiple jets observed, we can roughly estimate the value for the Froude number for each jet to be smaller than 1. This regime would thus be associated with intermittent internal wave breaking controlled by the mean shear generated by the jet. In order to confirm this scenario corresponding to the regime of mixing described in a recent study [41], we verify the stability of the interface deformation with respect to others mechanisms leading to mixing, Kelvin-Helmholtz (KH) or Holmboe (H) instabilities. We display the map of the Richardson number computed using the mean flow properties, $Ri_* = \frac{g'}{\delta h \nabla_z(\overline{u})}$ in Fig. 17, and we observe that the stability criteria for both these instabilities are valid. Indeed, we do not see regions with values of Ri_* smaller than 1/4 (KH criterion) or larger than 30 (H criterion).

In the context of our study dedicated to OGT, it is impossible for us to discriminate mixing induced by shear-free turbulence only with shear-free turbulence in the presence of weak jet-like mean flows. More precisely, we cannot know if shear-free turbulence is altered by the jets leading to a different entrainment rate, or if entrainment due to shear-free

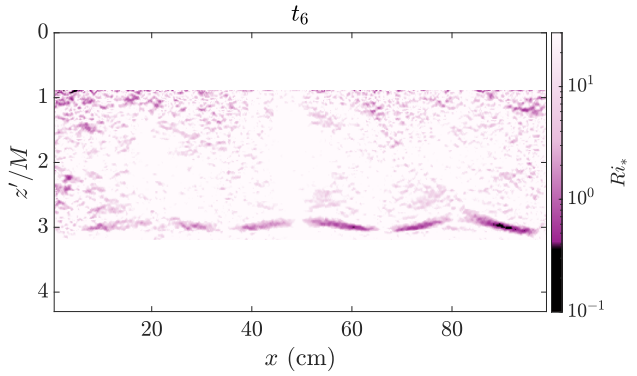

FIG. 17. Spatial map of the Richardson number, $Ri_* = \frac{g'}{\delta h \nabla_z(\overline{u})}$ based on the shear of the mean flow, $\nabla_z(\overline{u})$, interface thickness, δh and the the reduced gravity acceleration, g', at t_6 for S3 ($\Delta\rho_1$).

OGT can be added independently to the one due to turbulent plume. We consider that a better understanding of the amplification of U_{rms} at the interface could greatly help in answering the question.

VI. CONCLUSIONS

In this paper we have described the turbulent properties of shear-free turbulence induced by two different oscillating grid systems, in a homogeneous and a two-layer stratified fluid. In the case of OGT in a homogeneous fluid, our results are in good agreement with previous studies. We have improved the description of the turbulence decay with depth by considering a larger field of view, and we have been able to verify that the description of Matsunaga *et al.* [10] is better suited to model the fast decay far from the grid, although not perfectly adjusted in terms of fitting parameters. Our measurements have made a more complete description of all turbulent quantities based on a $k-\epsilon$ model, with a parametric form to prescribe them for grid Reynolds number in the range $[800, 12500]$. One noticeable improvement with previous studies is the description of the evolution with depth of the integral length scale L_{int} as a piece-wise linear function of z, with a specific depth H_s at which a discontinuity occurs. Consequently, we found that the eddy viscosity ν_t for OGT is better described as being almost constant over the depth range $[0, H_s]$, before decreasing as a power law in $z^{-3/2}$. The use of ν_t instead of k and ϵ could be very useful to study other problems in OGT, such as mixing or the transport of a second phase in general (pollutants, particles), and we hope this characterization will be of interest for future studies.

We have also characterized OGT in the case of a two-layer fluid. We verify that the turbulent flow far from the interface ($0 < z/h < 0.6$) is still comparable to OGT in a homogeneous fluid, although some variations of the fitting parameters with time can occur. Near the interface, differences with the case of an homogeneous fluid are observed. The loss of isotropy and the amplification of the turbulence near the interface is very similar to the observations made for a solid boundary [39] or in previous studies [23]. Peaks for the turbulent horizontal velocity, kinetic energy, and integral length are visible at a distance of L_{int}^{max} (max of the integral length with depth) or even less from the interface, before going to zero at the interface. Surprisingly, at the difference of the others turbulent quantities, the appropriate model for ν_t in this fluid environment is a constant value with depth, until reaching the interface where it goes to ν_f. The value is reasonably well predicted by the homogeneous model we presented.

Finally, we investigate the mixing that also takes place when studying OGT in a two-layer fluid. The results on the evolution of the interface with time and the entrainment law as a function of the Richardson number are comparable with past studies who systematically consider OGT in a homogeneous fluid as a reference for velocity and length scales [1, 15, 26]. Yet, the collapse of all observations on a simple law is not possible for various experimental cases with different strokes, frequencies or density jumps. The entrainment law of the interface might be a function of the Richardson number only, if the latter is associated to the turbulent flow properties measured at the interface and not from the properties deduced from homogeneous fluid cases. This 'local' Richardson number near the interface is clearly controlled by the turbulence at the interface. It is also a challenging quantity to assess since it must be measured in the region of the fluid with the strongest density and velocity gradients. Furthermore, there are different mechanisms at stake in such experimental studies that can alter the values of this Richardson number. It could be due shear-free turbulence only, or could be combined to other effects induced by weak mean flow resembling turbulent plumes. We suggest to investigate this question in future studies focusing on mixing of a two-layer fluid with OGT combined with other controlled flow features (turbulent plumes, mean circulation, etc.).

ACKNOWLEDGMENTS

The authors thank the technical support at IMFT for visualisations (S. Cazin, M.Marchal) and experimental setup (J.D. Barron, H.Ayrolles and F. Bergame). The authors also thank H. Michallet and M. Rastello for stimulating discussions.

---

[1] H. J. S. Fernando, Turbulent Mixing in Stratified Fluids, Annual Review of Fluid Mechanics **23**, 455 (1991).
[2] C. Wunsch and R. Ferrari, Vertical Mixing, Energy, and the General Circulation of the Oceans, Annual Review of Fluid Mechanics **36**, 281 (2004).
[3] H. E. Huppert, J. S. Turner, and M. A. Hallworth, Sedimentation and entrainment in dense layers of suspended particles stirred by an oscillating grid, Journal Fluid Mech **289**, 263 (1995).
[4] H. Michallet and M. Mory, Modelling of sediment suspensions in oscillating grid turbulence, Fluid Dynamics Research **35**, 87 (2004).
[5] J. Yan, N. S. Cheng, H. W. Tang, and S. K. Tan, Oscillating-grid turbulence and its applications: a review, Journal of Hydraulic Research **45**, 26 (2007).
[6] S. J. Bennett, Y. Hou, and J. F. Atkinson, Turbulence suppression by suspended sediment within a geophysical flow, Environmental Fluid Mechanics **14**, 771 (2014).
[7] S. M. Thompson and J. S. Turner, Mixing across an interface due to turbulence generated by an oscillating grid, Journal of Fluid Mechanics **67**, 349 (1975).
[8] E. J. Hopfinger and J. A. Toly, Spatially decaying turbulence and its relation to mixing across density interfaces, Journal of Fluid Mechanics **78**, 155 (1976).
[9] I. P. de Silva and H. J. Fernando, Some aspects of mixing in a stratified turbulent patch, Journal of Fluid Mechanics **240**, 601 (1992).
[10] N. Matsunaga, Y. Sugihara, T. Komatsu, and A. Masuda, Quantitative properties of oscillating-grid turbulence in a homogeneous fluid, Fluid Dynamics Research **25**, 147 (1999).
[11] M. Rastello, H. Michallet, and J. L. Marié, Sediment erosion in zero-mean-shear turbulence, Physics of Fluids **32**, 036601 (2020).
[12] M. Ura, T. Komatsu, and N. Matsunaga, Entrainment due to oscillating-grid turbulence in two-layered fluid, in *Turbulence Measurements and Flow Modeling* (1987) pp. 109–118.
[13] N. S. Cheng and A. W. K. Law, Measurements of Turbulence Generated By Oscillating Grid, Journal of Hydraulic Engineering **127**, 201 (2001).
[14] J. J. Orlins and J. S. Gulliver, Turbulence quantification and sediment resuspension in an oscillating grid chamber, Experiments in Fluids **34**, 662 (2003).
[15] R. I. Nokes, On the entrainment rate across a density interface, Journal of Fluid Mechanics **188**, 185 (1988).
[16] L. Verso, M. van Reeuwijk, and A. Liberzon, Steady state model and experiment for an oscillating grid turbulent two-layer stratified flow, Phys. Rev. Fluids **2**, 104605 (2017).
[17] E. J. Hopfinger and P. F. Linden, Formation of thermoclines in zero-mean-shear turbulence subjected to a stabilizing buoyancy flux, Journal of Fluid Mechanics **144**, 157 (1982).
[18] H. Rouse and J. Dodu, Diffusion turbulente à travers une discontinuité de densité, La Houille Blanche **4**, 522 (1955).
[19] P. F. Crapper and P. F. Linden, The structure of turbulent density interfaces, Journal of Fluid Mechanics **65**, 45 (1974).
[20] P. Linden, Mixing in stratified flows, Geophysical and Astrophysical Fluid Dynmaics **13**, 3 (1979).
[21] Y. Zellouf, P. Dupont, and H. Peerhossaini, Heat and mass fluxes across density interfaces in a grid-generated turbulence, International Journal of Heat and Mass Transfer **48**, 3722 (2005).
[22] J. D. Woods and V. Strass, The response of the upper ocean to solar heating II: The wind-driven current, Quarterly Journal of the Royal Meteorological Society **112**, 29 (1986).
[23] I. A. Hannoun, H. J. Fernando, and E. J. List, Turbulence structure near a sharp density interface, Journal of Fluid Mechanics **189**, 189 (1988).
[24] J. S. Turner, The influence of molecular diffusivity on turbulent entrainment across a density interface, Journal of Fluid Mechanics **33**, 639 (1968).
[25] H. J. Fernando and R. R. Long, The growth of a grid-generated turbulent mixed layer in a two-fluid system, Journal of Fluid Mechanics **133**, 377 (1983).
[26] I. A. Hannoun and E. J. List, Turbulent mixing at shear-free density interface, Journal of Fluid Mechanics **189**, 211 (1988).
[27] M. Mory, A model of turbulent mixing across a density interface including the effect of rotation, Journal of Fluid Mechanics **223**, 193–207 (1991).
[28] H. J. S. Fernando and J. C. R. Hunt, Turbulence, waves and mixing at shear-free density interfaces. part 1. a theoretical model, Journal of Fluid Mechanics **347**, 197–234 (1997).
[29] S. P. McKenna and W. R. McGillis, Observations of flow repeatability and secondary circulation in an oscillating grid-stirred tank, Physics of Fluids **16**, 3499 (2004).
[30] A. Al-Homoud and M. Hondzo, Energy dissipation estimates in oscillating grid setup: LDV and PIV measurements, Environmental Fluid Mechanics **7**, 143 (2007).

[31] M. Rastello, H. Michallet, and J. L. Marié, Sediment erosion in zero-mean-shear turbulence, Coastal Dynamics **94** (2017).
[32] M. W. McCorquodale and R. J. Munro, A method for reducing mean flow in oscillating-grid turbulence, Experiments in Fluids **59**, 1 (2018).
[33] S. B. Pope, *Turbulent folws*, cambridge ed., edited by C. U. Press (2000).
[34] R. J. Adrian and J. Westerweel, *Particle Image Velocimetry*, 1st ed. (Cambridge University Press, 2011) p. 558.
[35] S. J. Bennett, J. F. Atkinson, Y. Hou, and M. J. Fay, Turbulence modulation by suspended sediment in a zero mean-shear geophysical flow, Coherent Flow Structures at Earth's Surface **20**, 309 (2013).
[36] P. Doron, L. Bertuccioli, J. Katz, and T. R. Osborn, Turbulence Characteristics and Dissipation Estimates in the Coastal Ocean Bottom Boundary Layer from PIV Data, Journal of Physical Oceanography **31**, 2108 (2001).
[37] J. De Jong, L. Cao, S. H. Woodward, J. P. Salazar, L. R. Collins, and H. Meng, Dissipation rate estimation from PIV in zero-mean isotropic turbulence, Experiments in Fluids **46**, 499 (2009).
[38] D. Xu and J. Chen, Accurate estimate of turbulent dissipation rate using PIV data, Experimental Thermal and Fluid Science **44**, 662 (2013).
[39] M. W. McCorquodale and R. J. Munro, Experimental study of oscillating-grid turbulence interacting with a solid boundary, Journal of Fluid Mechanics **813**, 768–798 (2017).
[40] A. B. Shrinivas and G. R. Hunt, Confined turbulent entrainment across density interfaces, Journal of Fluid Mechanics **779**, 116 (2015).
[41] J. Herault, G. Facchini, and M. Le Bars, Erosion of a sharp density interface by a turbulent jet at moderate froude and reynolds numbers, Journal of Fluid Mechanics **838**, 631–657 (2018).

Appendix A: Depth profiles of turbulent quantities in homogeneous fluid for an other Reynolds number

In this section, depth profiles of turbulent quantities obtained for a Reynolds number, Re_g, of 7980 are shown (Stirring H3 in Table I). More precisely, depth profiles of the turbulent kinetic energy k (Fig. 18), the integral length-scale L_{int} (Fig. 19), the dissipation rate ϵ (Fig. 20) and the eddy viscosity ν_t (Fig. 21) are shown. This experiment was performed in setup 2, being different from the one used for the case presented in the main part of the paper. It highlights that our approach do not depend on the geometry of the tank. Moreover, in this setup, images where recorded in two different laser sheets. They were located at $x = L/4$ and $x = L/2$ from the border of the tank, where L is the width of the tank. Thus, we also illustrate that our approach describes the OGT in the whole tank.

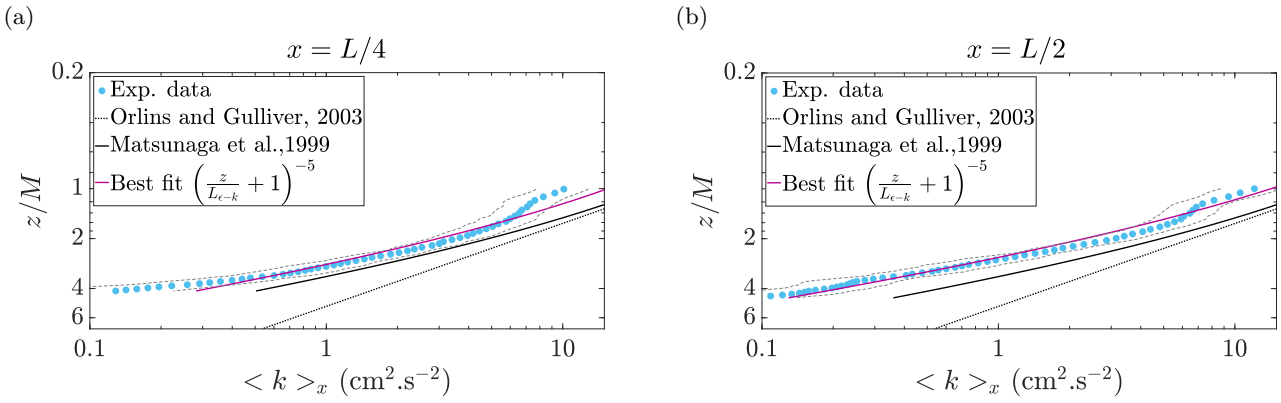

FIG. 18. Depth profiles of the turbulent kinetic energy, k, obtained in two laser sheets at (a) $x = L/4$ and (b) $x = L/2$ from the border of the tank. Symbols represent experimental data, with thin gray lines indicating the uncertainty in the values based on rms variations in k. Black lines represent models in eq. (2) and (3).

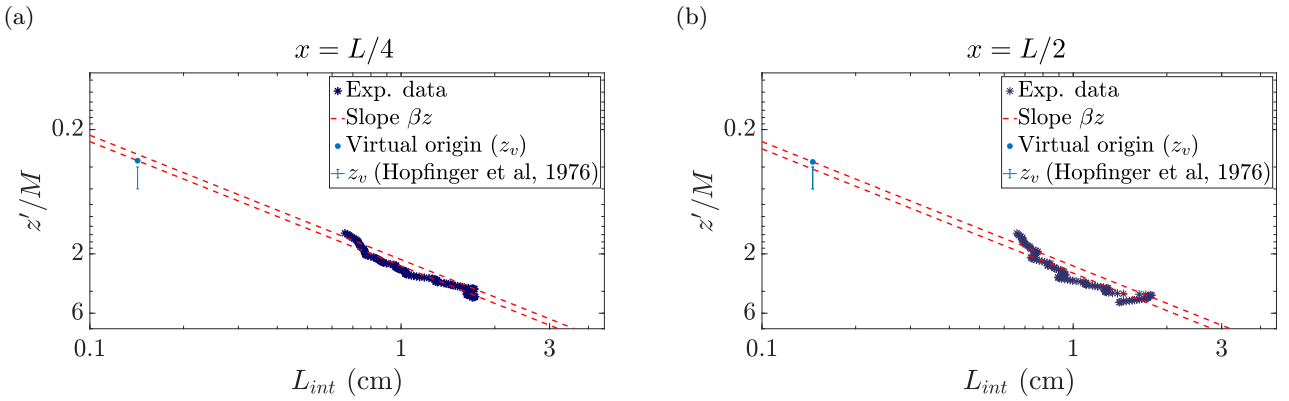

FIG. 19. Depth profiles of the integral length-scale, L_{int}, obtained in two laser sheets at (a) $x = L/4$ and (b) $x = L/2$ from the border of the tank. The blue diamond is the virtual origin from the experimental data. The error-bar is the virtual origin from [8]. Red dash lines are eq. (6) for two proportionality constants.

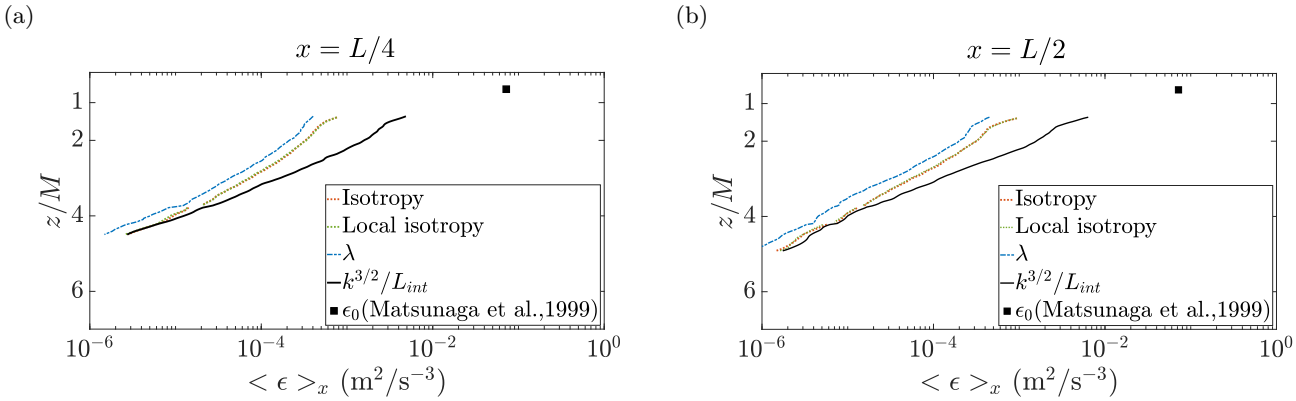

FIG. 20. Vertical profiles of the dissipation rate, ϵ, calculated from four definitions with different assumptions. They was obtained in two laser sheets at (a) $x = L/4$ and (b) $x = L/2$ from the border of the tank.

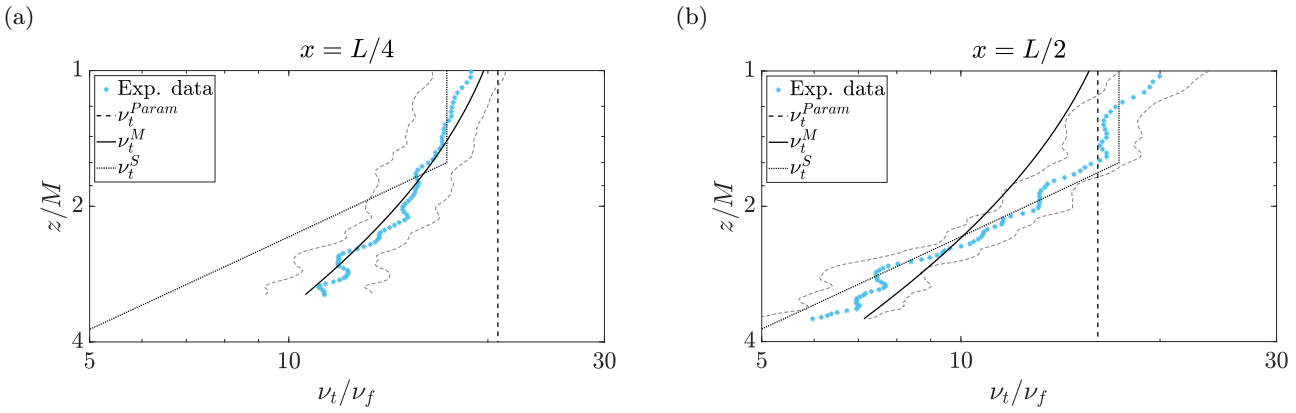

FIG. 21. Depth profiles of the eddy viscosity, ν_t, obtained in two laser sheets at (a) $x = L/4$ and (b) $x = L/2$ from the border of the tank. ν_t is normalized by the fluid kinematic viscosity ν_f. Symbols are experimental data with thin blue lines indicating the uncertainty in the values. Black lines are the parametric laws from equations (9) to (11).

Appendix B: Details on dissipation rate definitions

The dissipation rate, ϵ, which characterizes the turbulence decay is defined by the velocity gradients as

$$\epsilon = \nu_f \left(\frac{\partial u_i'}{\partial x_j} \frac{\partial u_i'}{\partial x_j} + \frac{\partial u_i'}{\partial x_j} \frac{\partial u_j'}{\partial x_i} \right) \tag{B1}$$

From experimental data, access to the three components of the velocity is not always possible. Therefore, several methods exist to determine the dissipation rate. They are listed below:

- Assuming isotropy (i.e. the 3 velocity components are equal), the definition eq. (B1) becomes

$$\epsilon = 15\,\nu_f \left(\frac{\partial u'}{\partial x} \right)^2 \tag{B2}$$

- Assuming local isotropy (i.e. 2 velocity components are equal, u' et v' in our case) and using the continuity equation ($\frac{\partial u'}{\partial x} + \frac{\partial v'}{\partial y} + \frac{\partial w'}{\partial z} = 0$), the definition eq. (B1) becomes

$$\epsilon = 4\,\nu_f \left[\left(\frac{\partial u'}{\partial x} \right)^2 + \left(\frac{\partial w'}{\partial z} \right)^2 + \frac{\partial u'}{\partial x} \frac{\partial w'}{\partial z} + \frac{3}{4} \left(\frac{\partial U'}{\partial z} + \frac{\partial w'}{\partial x} \right)^2 \right]. \tag{B3}$$

  This assumption is usually done in case of PIV 2D-2C measurements [30, 36, 37]. As a remark, Al-Homoud and Hondzo [30] and Doron *et al.* [36] found a factor of 3 in front of terms 1, 2 and 5 of the right-hand member of eq. (B3). It is probably an error due to an omission of the factor 2 for the term $\frac{\partial v'}{\partial y}$ in the definition of ϵ. By doing the calculation again, we find the same expression as De Jong *et al.* [37].

- From the integral lengthscale, L_{int}, ϵ is expressed as follow [4, 8, 33, 34]

$$\epsilon = \frac{k^{3/2}}{L_{int}}. \tag{B4}$$

- From the Taylor scale, L_T, ϵ is expressed as follow [34]

$$\epsilon = 15\nu_f \frac{u'^2}{L_T^2}. \tag{B5}$$

- From the power density spectrum, PDS, in the inertial domain, ϵ is expressed as follows [10, 38]

$$PDS = C_\eta \epsilon^{2/3} k_x^{-5/3}. \tag{B6}$$

  As a remark, the inertial range should be covered over at least one or two decades to minimize the uncertainty on the slope and thus on ϵ.

- From the longitudinal structure function at order 2, $D_{LL}(r) =$. It corresponds to the covariance between the velocity difference between two positions in space x and $x + dr$. Based on the first and the second Kolmogorov's similarity hypotheses, we can show that the structure function depends only on the dissipation rate such that [33, 38]

$$\epsilon = \frac{1}{r} \left(\frac{D_{LL}(r)}{C} \right)^{3/2} \quad with \quad C = 2.12. \tag{B7}$$

  As a remark, in the case of homogeneous and/or isotropic flows, the authors use the instantaneous velocity field to compute D_{LL} and deduce ϵ. Indeed, in these cases, the mean velocity is translation invariant (or equal to zero in the case of isotropic flow). Therefore, D_{LL} being deduced from a difference between two positions in space, using the instantaneous velocity field of the fluctuating one leads to the same expression. In our case, D_{LL} is directly calculated from the fluctuating velocity field.

Appendix C: Comparison of the turbulent structure near the grid in homogeneous fluid and two-layer fluid

Here we present maps of the horizontal fluctuation velocity, used to calculate the integral length scale. In a homogeneous fluid, the signature of the grid, with the presence of jets under each grid bar, is clearly visible (Fig.22(a)) while in a two-layer fluid, two more prominent structures appear (Fig.22(b)). These differences in the flow could explain the different behavior observed for L_{int}, in particular its discontinuity at depth H_s in a homogeneous fluid. As a remark, in a homogeneous fluid, we observed the same signature of the grid for all cases. In two-layer fluid, the number of structures below the grid depends on the grid frequency, but they are always larger than the size of the grid bars. We could not explain the grid frequency dependence, but we verified that these structures are not grid eigenmodes.

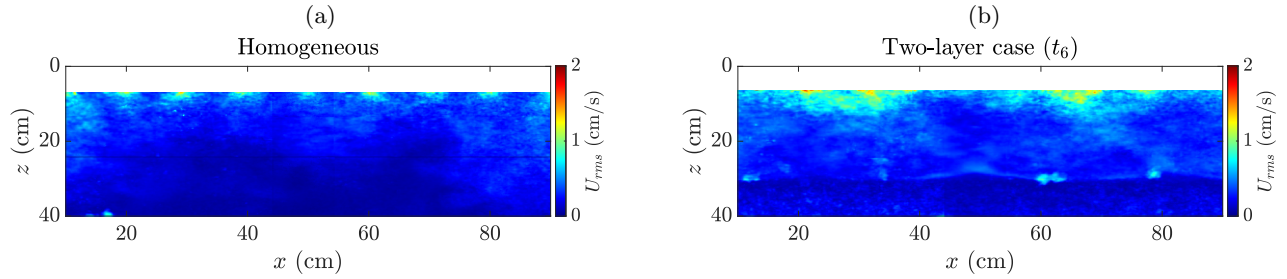

FIG. 22. Map of horizontal fluctuating velocity in (a) homogeneous fluid (case H12) and (b) two-layer fluid (case S3 at t_6).

Appendix D: Internal waves signatures in a two-layer fluid for case S3

We discuss here some results on the internal waves dynamics near the interface for one specific case, S3 at time t_2. Similar results have been obtained at other times and for the other cases.

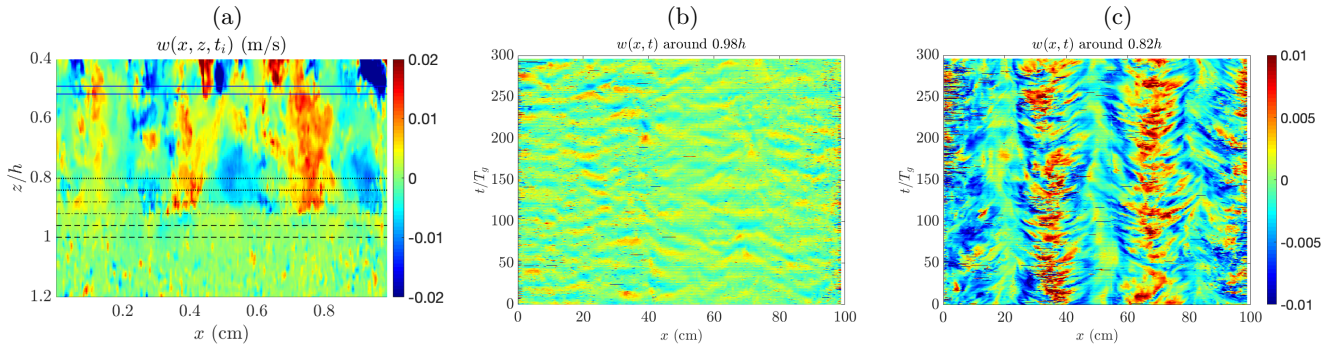

FIG. 23. Case S3, t_2. (a) Instantaneous vertical velocity field, $w(x,z,t_i)$ around $t_i/Tg \simeq 150$, with indications on the domains for the extracted time series in (b) and (c), centered around $z/h \simeq 0.98$ and $z/h \simeq 0.82$ respectively (between black lines, vertical extent of approximately $0.04h$). The colorbars for (b) and (c) are the same.

We first present in Fig. 23 the dataset investigated for internal waves dynamics. From instantaneous velocity measurements (panel a), we extract time series of horizontal and vertical velocities at some depth, with some averaging in the vertical in between discontinuous black lines (panel a), to reduce the level of noise. Two resulting time series are shown in panels b and c for instance. An extra time series is extracted far away from the interface ($z/h \simeq 0.5$ in between blue lines in panel a), which corresponds to a region described in the manuscript where the dynamics is similar to the case of a homogeneous fluid. Near the interface ($z/h \simeq 0.98$), the amplitude of the flow features are of the order of $2.5\,10^{-3}$ m/s whereas further away ($z/h \simeq 0.82$), the amplitude of the more complex flow features corresponding to the superposition of waves, mean flow and turbulent structures is four times larger.
From these time series at four depths above the interface, we compute the density spectrum with respect to time of the velocity components at each horizontal location, and average these quantities over the horizontal, noted $< E^t_{ww} >_x$ and $< E^t_{uu} >_x$, function of f as shown in Fig. 24(a). Alternatively, we can also compute the density spectrum with respect to the horizontal coordinates at each frame, and average these quantities over time, noted $< E^x_{ww} >_t$ and

$< E^x_{uu} >_t$, function of k_x as shown in Fig. 24(b). Density spectra in two-dimensions, functions of f and k_x for the whole time series could also be extracted but are quite noisy and tougher to interpret, an example is shown for the vertical velocity (E_{ww}) at $z/h \simeq 0.90$ in Fig. 24(c). One can notice that the signature of internal waves very near

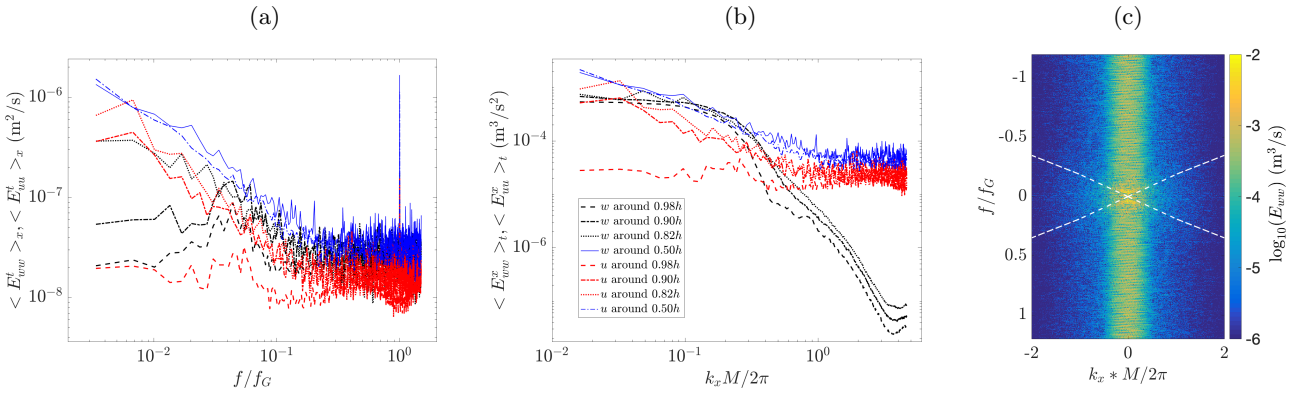

FIG. 24. Case S3, t_2. (a) Temporal and (b) spatial spectra of the times series extracted for u and w in the domains shown in Fig. 23, averaged over the (a) horizontal coordinate or (b) time. (c) Example of a two-dimensional spectrum for the vertical component of the velocity extracted $z/h \simeq 0.9h$. White dashed lines indicates the dispersion relation for internal waves in a two-layer fluid.

the interface (around $z/h \simeq 0.9$) is the main contribution to the spectra of both horizontal and vertical velocities in the range $[0.01, 0.06]f_G$ ($[0.02, 0.12]$ Hz with $f_G = 2$Hz in the case shown, S3). Based on the dispersion relation of internal waves in a two-layer fluid, this corresponds to wavelength of the order of 0.1 to 1m, in good agreement with observations from Fig.23. This is further confirm by the fact that the energy associated is concentrated near the spectral domain for the dispersion relation of waves in an idealized two-layer fluid

$$\omega = \sqrt{\frac{\Delta\rho g}{\bar{\rho}} \frac{k_x}{\coth(k_x h_1) + \coth(k_x h_2)}} \tag{D1}$$

(white dashed lines in Fig. 24(c)).

Overall, the energy of the signal for internal waves is smaller than the one due to turbulence above the interface ($z/h \simeq 0.5$), or at most of comparable energy when limiting the analysis to this specific frequency-wavenumber spectral range.

Appendix E: Depth profiles of turbulent quantities in two-layer fluid for case S1

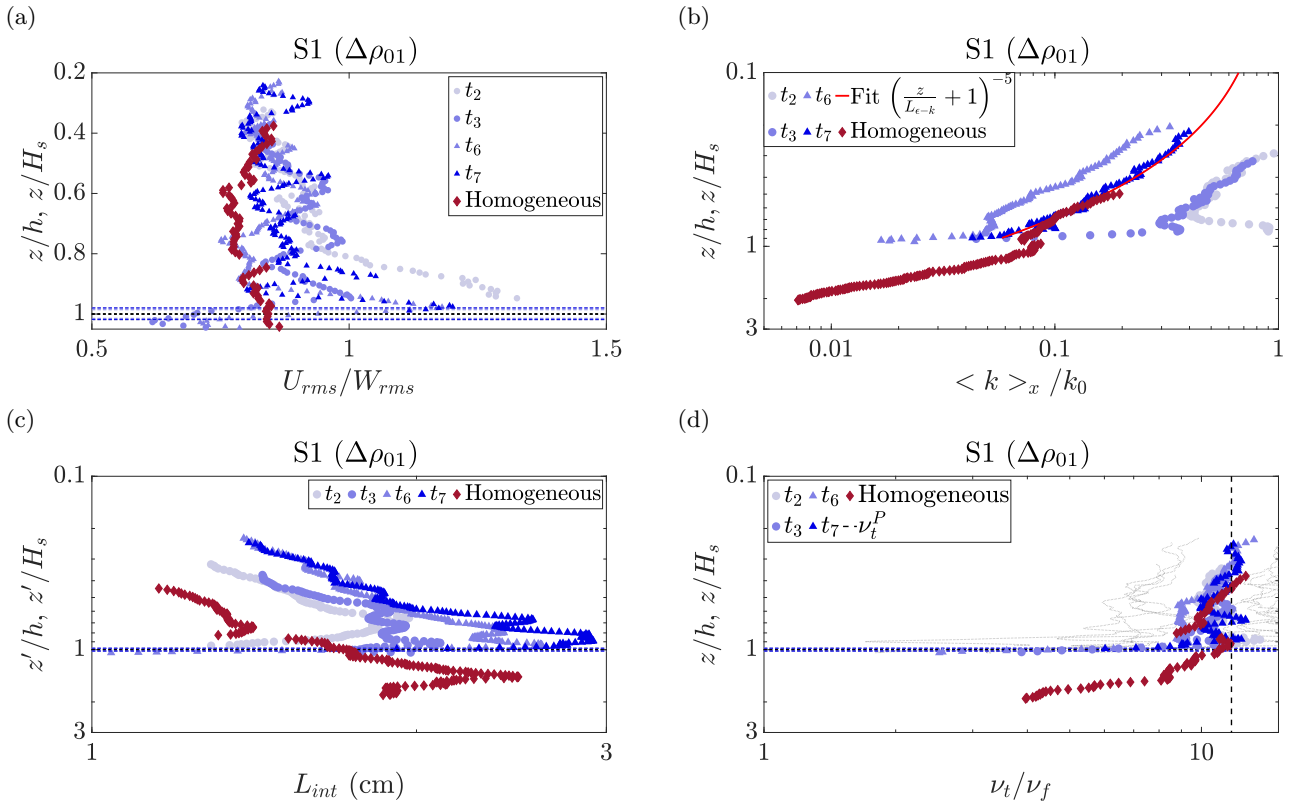

FIG. 25. Depth profiles of (a) the isotropy degree, (b) TKE, (c) integral length-scale, and (d) turbulent eddy diffusivity, with the z-axis starting from the top position of the grid normalized by h for the two-layer fluid and by H_s for the homogeneous fluid; for case S1 ($\Delta\rho_1$).

Appendix F: Mixing - complementary results

Related to the temporal evolution of the position of the interface, we try to estimate the dependency of C_B in eq.(14) with the forcing parameters. We present four possible combinations in Fig. 26.

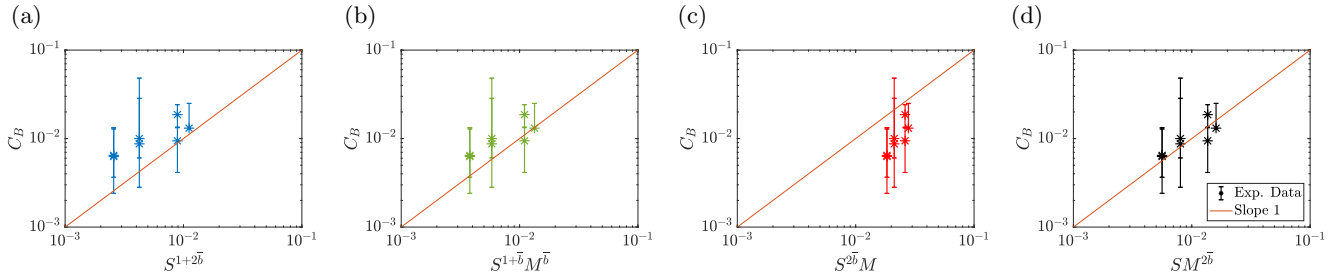

FIG. 26. Scaling laws of the parameter C_B as a function of the characteristic length scales of the device (S the stroke and M the grid mesh). Symbols are experimental data and red line is the slope 1. The mean value of $\bar{b} = 0.198$ was taken.

Regarding the temporal evolution of the interface thickness, we display it normalized by the position of the interface or the integral length in Fig. 27 (a) and (b) respectively. It must be reminded that δh is determined using conductivity measurements, being instantaneous density profiles. But due to local and intermittent distortions of the interface, regarding only instantaneous density profiles can lead to some aberrant points as already noted in Hannoun and List [26]. This can explain some scattering of the points in Fig. 27, even if the steady state should be reached (S4, $\Delta\rho_2$).

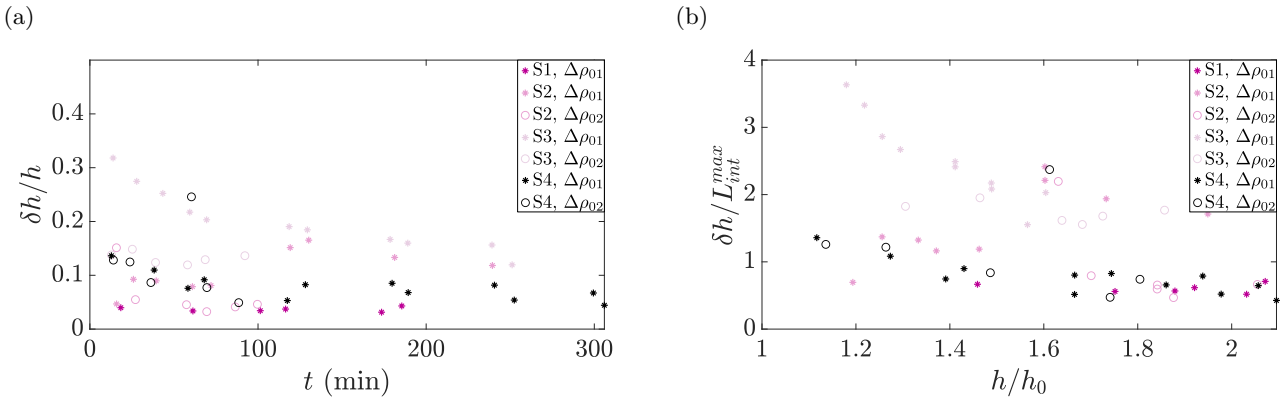

FIG. 27. (a) Time evolution of the interface thickness, δh, normalized by the interfacial position, h. (b) Evolution of δh, normalized by the maximum value of the integral length-scale L_{int}^{max}, as a function of h normalized by the initial interfacial position, h_0.